Single-cell analysis reveals fibroblast clusters linked to immunotherapy resistance in cancer

Yann Kieffer, Hocine Rachid Hocine, Géraldine Gentric, Floriane Pelon, Charles Bernard, Brigitte Bourachot, Sonia Lameiras, Luca Albergante, Claire Bonneau, Alice Guyard, et al.

Author Manuscript Published OnlineFirst on May 20, 2020; DOI: 10.1158/2159-8290.CD-19-1384
Author manuscripts have been peer reviewed and accepted for publication but have not yet been edited.

Single-cell analysis reveals fibroblast clusters linked to immunotherapy resistance in cancer

Yann Kieffer[1,2,11], Hocine R. Hocine[1,2,11], Géraldine Gentric[1,2,12], Floriane Pelon[1,2,12], Charles Bernard[1,2,12], Brigitte Bourachot[1,2], Sonia Lameiras[3], Luca Albergante[4,5], Claire Bonneau[1,2,6], Alice Guyard[7], Karin Tarte[8], Andrei Zinovyev[4,5], Sylvain Baulande[3], Gerard Zalcman[1,2,9], Anne Vincent-Salomon[10] and Fatima Mechta-Grigoriou[1,2,*]

[1] Institut Curie, Stress and Cancer Laboratory, Equipe labélisée par la Ligue Nationale contre le Cancer, PSL Research University, 26, rue d'Ulm, F-75248 Paris, France

[2] Inserm, U830, 26, rue d'Ulm, Paris, F-75005, France

[3] ICGex Next-Generation sequencing platform, Institut Curie, SIRIC, 26, rue d'Ulm, Paris, F-75005, France

[4] Institut Curie, Inserm, U900, PSL Research University, F-75248 Paris, France

[5] Mines ParisTech, CBIO-Centre for Computational Biology, F-75006 Paris, France

[6] Department of Surgery, Institut Curie Hospital Group, 35 rue Dailly, 92210 Saint-Cloud, France

[7] Department of pathology Bichat Claude Bernard Hospital Group, Paris Diderot University, 46, rue Henri Huchard, 75877 PARIS cedex 18, France

[8] UMR U1236-MICMAC, Immunology and Cell Therapy Lab, Rennes University, 2, avenue du Pr Léon Bernard, 35043 Rennes, France

[9] Thoracic Oncology Department, CIC 1425-CLIP2, Bichat Claude Bernard Hospital Group, Paris Diderot University, 46, rue Henri Huchard, 75877 PARIS cedex 18, France

[10] Department of Diagnostic and Theragnostic Medicine, Institut Curie Hospital Group, 26, rue d'Ulm, F-75248 Paris, France

[11,12] These authors contributed equally to this work as 1st and 2nd authors, respectively

* Correspondence: Fatima Mechta-Grigoriou (ORCID Number: 0000-0002-3751-6989) Phone: +33 (0)1 56 24 66 53; Fax: +33 (0)1 56 24 66 50; E-mail address: fatima.mechta-grigoriou@curie.fr

Running title

FAP$^+$ CAF diversity and immunotherapy response

Emails Mailing address, and telephone number of each author:

* Yann KIEFFER: yann.kieffer@curie.fr. Stress and Cancer laboratory. Institut Curie, U830 Inserm, 26, rue d'Ulm, F-75248 Paris, France +33 (0)1 56 24 66 40

* Hocine R. HOCINE: HocineR@mskcc.org. Stress and Cancer laboratory. Institut Curie, U830 Inserm, 26, rue d'Ulm, F-75248 Paris, France +1 929 810 9316

* Géraldine GENTRIC : geraldine.gentric@curie.fr. Stress and Cancer laboratory. Institut Curie, U830 Inserm, 26, rue d'Ulm, F-75248 Paris, France. +33 (0)1 56 24 67 27

* Floriane PELON : Floriane.pelon@curie.fr. Stress and Cancer laboratory. Institut Curie, U830 Inserm, 26, rue d'Ulm, F-75248 Paris, France. + 33 (0)1 43 79 35 17

* Charles BERNARD : charles.bernard@cri-paris.org. Stress and Cancer laboratory. Institut Curie, U830 Inserm, 26, rue d'Ulm, F-75248 Paris, France. +33 (0)1 44 27 34 70

* Brigitte BOURACHOT : brigitte.bourachot@curie.fr. Stress and Cancer laboratory. Institut Curie, U830 Inserm, 26, rue d'Ulm, F-75248 Paris, France. +33 (0)1 56 24 67 27

* Sonia LAMEIRAS : Sonia.Lameiras@curie.fr. ICGex Next-Generation sequencing platform, Institut Curie, SIRIC, 26, rue d'Ulm, Paris, F-75005, France. +33 (0) 1 56 24 67 38

* Luca ALBERGANTE : lucas.albergante@curie.fr. Institut Curie, Inserm, U900, Mines ParisTech, CBIO-Centre for Computational Biology, 26, rue d'Ulm, Paris, F-75005, France. +44 (0)7576339521

* Claire BONNEAU : Claire.Bonneau@curie.fr. Department of Surgery, Institut Curie Hospital Group, 35 rue Dailly, 92210 Saint-Cloud, France. +33 (0) 1 47 11 36 76

* Alice GUYARD : alice.guyard@aphp.fr. Department of pathology Bichat Claude Bernard Hospital Group, Paris Diderot University, 46, rue Henri Huchard, 75877 PARIS cedex 18, France. +33 1 40 25 75 02

* Karin TARTE: karin.tarte@univ-rennes1.fr. UMR U1236-MICMAC, Immunology and Cell Therapy Lab, Rennes University, 2, avenue du Pr Léon Bernard, 35043 Rennes, France. +33 (0)2 232 345 12

* Andrei ZINOVYEV : Andrei.Zinovyev@curie.fr. Institut Curie, Inserm, U900, Mines ParisTech, CBIO-Centre for Computational Biology, 26, rue d'Ulm, Paris, F-75005, France. +33 (0) 1 56 24 69 91

* Sylvain BAULANDE : Sylvain.Baulande@curie.fr. ICGex Next-Generation sequencing platform, Institut Curie, SIRIC, 26, rue d'Ulm, Paris, F-75005, France. +33 (0) 1 56 24 67 38

* Gerard ZALCMAN : gerard.zalcman@aphp.fr. Thoracic Oncology Department, CIC 1425-CLIP2, Bichat Claude Bernard Hospital Group, Paris Diderot University, 46, rue Henri Huchard, 75877 PARIS cedex 18, France. +33 1 40 25 75 02

* Anne VINCENT-SALOMON: anne.salomon@curie.fr. Department of Diagnostic and Theragnostic Medicine, Institut Curie Hospital Group, 26, rue d'Ulm, F-75248 Paris, France. +33 (0) 1 44 32 42 15

* Fatima MECHTA-GRIGORIOU : fatime.mechta-grigoriou@curie.fr. Stress and Cancer laboratory. Institut Curie, U830 Inserm, 26, rue d'Ulm, F-75248 Paris, France. +33 (0) 1 56 24 66 53

CONFLICT OF INTEREST

G.Z. served in scientific advisory boards for Bristol-Myers-Squibb (BMS), Merck Sharp & Dohme (MSD), Astra-Zeneca firms, manufacturing checkpoint inhibitors drugs, and perceived reimbursement for international meetings attendance by BMS, Astra-Zeneca and Roche. He served as investigator in immuno-oncology clinical trials sponsored by Roche, MSD, BMS and Astra-Zeneca. F.M-G. received research support from Innate-Pharma, Roche and BMS. Other authors declare no potential conflict of interest.

KEYWORDS

Heterogeneity, Stroma, Resistance to Immunotherapy, Breast and lung Cancer, Melanoma

ABSTRACT

A subset of Cancer-Associated Fibroblasts (FAP^+/CAF-S1) mediates immunosuppression in breast cancers (BC), but its heterogeneity and its impact on immunotherapy response remain unknown. Here, we identify 8 CAF-S1 clusters by analyzing more than 19000 single CAF-S1 fibroblasts from BC. We validate the 5 most abundant clusters by flow cytometry and *in silico* analyses in other cancer types, highlighting their relevance. Myofibroblasts from clusters 0 and 3, characterized by extra-cellular matrix proteins and TGFβ signaling respectively, are indicative of primary resistance to immunotherapies. Cluster 0/ecm-myCAF up-regulates PD-1 and CTLA-4 protein levels in regulatory T lymphocytes (Tregs), which in turn increases CAF-S1 cluster 3/TGFβ-myCAF cellular content. Thus, our study highlights a positive feedback loop between specific CAF-S1 clusters and Tregs and uncovers their role in immunotherapy resistance.

STATEMENT OF SIGNIFICANCE

Our work provides a significant advance in characterizing and understanding FAP^+ CAF in cancer. We reach a high resolution at single cell level, which enabled us to identify specific clusters associated with immunosuppression and immunotherapy resistance. Identification of cluster-specific signatures paves the way for therapeutic options in combination with immunotherapies.

INTRODUCTION

Cancer-Associated Fibroblasts (CAF) represent one of the most abundant components in adenocarcinomas and play key pro-tumorigenic functions (1-6). It is now recognized that CAF are heterogenous and that distinct CAF subsets can be defined based on expression of specific markers (7-17). Recently, studies based on immunocompetent mouse models reported that CAF expressing the Fibroblast Activation Protein (FAP) marker are associated with an immunosuppressive environment (9,18-24). Moreover, the concomitant study of 6 markers, including FAP, smooth-muscle α actin (SMA) and integrin β1 (CD29), revealed the existence of 4 CAF subsets, referred to as CAF-S1 to -S4, in human breast and ovarian cancers (8,10). While CAF-S2 (FAP^{Neg} $CD29^{Low}$ SMA^{Neg}) and CAF-S3 (FAP^{Neg} $CD29^{Med}$ SMA^{Neg}) fibroblasts are also detected in healthy tissues and could be reminiscent of normal fibroblasts, CAF-S1 (FAP^{High} $CD29^{Med\text{-}High}$ SMA^{High}) and CAF-S4 (FAP^{Neg} SMA^{High} $CD29^{High}$) myofibroblasts cells are restricted to cancer and metastatic lymph nodes. CAF-S1 fibroblasts are defined by extracellular matrix and inflammation signatures, and CAF-S4 are characterized by a perivascular signature (8,10). Both CAF-S1 and CAF-S4 promote metastases through complementary mechanisms (17). In contrast, while CAF-S1 promote immunosuppression in human cancer, CAF-S4 do not (8). Specifically, CAF-S1 fibroblasts stimulate immunosuppression by increasing attraction, survival and overall content of $CD4^+$ $CD25^+$ $FOXP3^+$ regulatory T cells (Tregs) in tumor micro-environment (8,10). In line with these observations, FAP^{High} CAF have also been suspected to contribute to primary resistance to immunotherapies (7,9,25). However, to our knowledge, the direct role of FAP^{High} CAF in immunotherapy resistance has not yet been addressed in human cancer. This observation, coupled with the recent finding that FAP^{High} CAF-S1 fibroblasts exert their immunosuppressive function through a multi-step mechanism (8,10), prompted us to study their heterogeneity and specific roles in primary resistance to immunotherapy in cancer patients.

In recent years, single-cell RNA sequencing (scRNA-seq) has been developed to analyze intratumoral heterogeneity. We used this new approach to address the heterogeneity of the

FAP^{High} CAF-S1 immunosuppressive subpopulation. We performed scRNA-seq of more than 19000 CAF-S1 fibroblasts isolated from 8 primary breast cancers (BC) and identified 8 different CAF-S1 clusters. Among them, 3 CAF-S1 clusters (1, 2, 5) belong to the inflammatory ("iCAF") subgroup and 5 CAF-S1 clusters (0, 3, 4, 6, 7) to the myofibroblastic ("myCAF") subgroup, iCAF and myCAF having been previously identified in pancreatic cancer (7,16,26). The 8 CAF-S1 clusters identified here are characterized by high expression of genes coding extra-cellular matrix (ECM) proteins (cluster 0), detoxification pathway (cluster 1), interleukin-signaling (cluster 2), Transforming Growth Factor β (TGFβ) signaling pathway (cluster 3), wound healing (cluster 4), interferon γ (IFNγ) (cluster 5), interferon αβ (IFNαβ) (cluster 6), acto-myosin pathway (cluster 7). Accordingly, we annotated them as follows: ecm-myCAF (cluster 0), detox-iCAF (cluster 1), IL-iCAF (cluster 2), TGFβ-myCAF (cluster 3), wound-myCAF (cluster 4), IFNγ-iCAF (cluster 5), IFNαβ-myCAF (cluster 6) and acto-myCAF (cluster 7). We confirmed the existence and the relative proportions of the 5 most abundant CAF-S1 clusters (representing up to 91% of sequenced cells) in BC by multicolor flow cytometry using a combination of specific markers. Moreover, we validated the existence of these 5 CAF-S1 cellular clusters in head and neck squamous cell carcinoma (HNSCC) and in non-small cell lung cancer (NSCLC) by analyzing publicly available scRNA-seq data, demonstrating the relevance of these CAF-S1 clusters across different cancer types. In addition, we uncovered that the abundance of two CAF-S1 clusters of the myCAF subgroup, namely ecm-myCAF and TGFβ-myCAF, is significantly correlated with an immunosuppressive environment, whereas the content in detox-iCAF and IL-iCAF is not. Indeed, ecm-myCAF and TGFβ-myCAF clusters are enriched in tumors with high levels of PD-1$^+$, CTLA-4$^+$ and TIGIT$^+$ CD4$^+$ T lymphocytes (themselves enriched in Tregs), and low fraction of CD8$^+$ T lymphocytes. Importantly, we found that, at diagnosis, these CAF-S1 clusters are associated with primary resistance to immunotherapies in both melanoma and NSCLC patients. In agreement with these findings, ecm-myCAF increase the fraction of FOXP3^{high} T cells and stimulate both PD-1 and CTLA-4 protein levels at the surface of CD4$^+$ CD25$^+$ T lymphocytes, which in turn increase the proportion of TGFβ-myCAF. Thus, our study

uncovers a positive feedback loop between the immunosuppressive ecm-myCAF and TGFβ-myCAF CAF-S1 clusters and Tregs that could participate in immunotherapy resistance.

RESULTS

Distinct cellular clusters are identified within the immunosuppressive CAF-S1 subset by single-cell approach

We used single-cell RNA sequencing (scRNA-seq) to investigate cellular heterogeneity within the CAF-S1 immunosuppressive subset. We isolated CAF-S1 fibroblasts from human BC (see description of prospective cohort 1 in **Table S1**) by FACS as previously described (8,10,17). In brief, from freshly resected tumors, we first excluded debris, dead cells, doublets, epithelial ($EPCAM^+$), hematopoietic ($CD45^+$), endothelial ($CD31^+$) and red blood ($CD235a^+$) cells (**Fig. S1A**). We considered $EPCAM^-$ $CD45^-$ $CD31^-$ $CD235a^-$ as the fraction of cells enriched in fibroblasts and next performed FAP and CD29 staining (**Fig. S1A**), which enabled us to distinguish CAF-S1 (FAP^{High} $CD29^{Med\text{-}High}$) from the other CAF subpopulations (CAF-S2: FAP^{Neg} $CD29^{Low}$; CAF-S3: FAP^{Neg} $CD29^{Med}$; CAF-S4: FAP^{Neg} $CD29^{High}$) (**Fig. S1A**), as previously established in (8,10). We then performed scRNA-seq of 18 805 CAF-S1 fibroblasts from 7 BC patients prior any treatment (**Fig. 1**). After quality control, 18 296 CAF-S1 fibroblasts with a median of 2428 genes detected per cell were conserved for further analyses**.** Unsupervised graph-based clustering identified 8 CAF-S1 clusters, visualized with the Uniform Manifold Approximation and Projection (UMAP) algorithm (**Fig. 1A).** All clusters were found in most patients from Lum and TN BC subtypes, albeit it at varying levels (**Fig. 1B, C**). No individual cluster was associated with a particular phase of cell cycle or with high proliferation (**Fig. S1B**), as shown using G1/S and G2/M gene signatures (27). We confirmed the detection of these different CAF-S1 cellular clusters using the Label Transfer algorithm (28). Indeed, this algorithm successfully transferred with high prediction scores all the 8 cluster labels in an independent CAF-S1 scRNA-seq dataset, newly generated from an 8^{th} BC patient (**Fig. S1C**).

Differential gene expression analyses revealed that each cluster was characterized by a specific transcriptional profile (**Data S1**). Cluster 0 was associated with ECM remodeling, cell-substrate adhesion and collagen formation; cluster 1 with detoxification and inflammatory response; cluster 2 with response to growth factor, TNF signaling and Interleukin pathway;

cluster 3 with TGFβ signaling pathway and matrisome; cluster 4 with assembly of collagen fibrils and wound healing; cluster 5 with response to Interferon γ (IFNγ and cytokine-mediated signaling pathway; cluster 6 with IFNα/β signaling; and cluster 7 with acto-myosin complex (**Data S1**). As examples, we found high expression of *LRRC15 (Leucine Rich Repeat Containing 15*), a marker recently identified in CAF from pancreatic cancer (29) and *GBJ2* (*Gap junction protein beta 2*) in cluster 0, *ADH1B* (*Alcohol dehydrogenase 1*) and *GPX3* (*Glutathione peroxidase 3*) in cluster 1, *RGMA* (Repulsive guidance molecule BMP co-receptor) and *SCARA5 (Scavenger receptor class A member 5)* in cluster 2, *CST1* (*Cystatin*) and *TGFβ1* in cluster 3, *SEMA3C* (*Semaphorin 3C*) and *SFRP4 (Secreted Frizzled Related Protein 4*) in cluster 4, *CCL19* and *CCL5* (*CC motif chemokine ligand 19 and 5)* in cluster 5, *IFIT3* (*Interferon induced protein with tetratricopeptide repeats 3*) and *IRF7* (*Interferon regulatory factor 7*) in cluster 6, *GGH* (*γ-glutamyl hydrolase*) and *PLP2* (*Proteolipid protein 2*) in cluster 7 (**Fig. 1D**). Interestingly, in human BC, we were able to distinguish the myofibroblastic ("myCAF") and inflammatory ("iCAF") fibroblast subgroups (**Fig. 1E, F**), previously identified in FAP^+ fibroblasts from pancreatic cancer (7,16,26). CAF-S1 clusters 1, 2 and 5 were identified as iCAF and clusters 0, 3, 4, 6, and 7 as myCAF (**Fig. 1E, F**). Consistent with data from pancreas cancer, iCAF showed high expression of chemokines and pro-inflammatory molecules such as *CXCL12 (CXC motif chemokine ligand 12)* and *SOD2 (Superoxide dismutase 2)* (**Fig. 1E**), while myCAF expressed myofibroblast markers, including *COL1A2 (Collagen type 1 alpha 2 chain)* and *TAGLN* (*Transgelin*) (**Fig. 1F**). In addition, we observed that the iCAF cluster 5 expressed high levels of *CD74*, encoding *Major Histocompatibility Class (MHC) II invariant chain* (**Fig. 1G**). *CD74* was recently shown to be specifically expressed in the antigen-presenting CAF ("apCAF") in pancreatic cancer (16), suggesting that the CAF-S1 cluster 5 might be reminiscent of such apCAF (**Fig. 1G**). To summarize, we identified 8 different CAF-S1 clusters in BC. Clusters 1, 2 and 5 belong to the iCAF subgroup, with cluster 5 that might correspond to the apCAF cluster, whereas clusters 0, 3, 4, 6 and 7 belong to the myCAF subgroup. Moreover, iCAF clusters are characterized by detoxification (cluster 1), response to stimuli (cluster 2), IFNγ and cytokines

(cluster 5); and myCAF clusters by ECM (cluster 0), TGFβ (cluster 3), wound-healing (cluster 4), IFNα/β (cluster 6) and acto-myosin (cluster 7). Accordingly, we proposed the following nomenclature for these different FAP^{High} CAF-S1 clusters: cluster 0 = ecm-myCAF, cluster 1 = detox-iCAF, cluster 2 = IL-iCAF, cluster 3 = TGFβ-myCAF, cluster 4 = wound-myCAF, cluster 5 = IFNγ-iCAF, cluster 6 = IFNαβ-myCAF and cluster 7 = acto-myCAF.

Finally, we wondered whether these CAF-S1 clusters accumulate differentially in the different BC subtypes. Since we performed analysis on patients prior any treatment, the fresh samples collected for scRNA-seq were mostly collected from Luminal (Lum) patients, the HER2 and TN BC patients being preferentially treated in neoadjuvant settings. Consequently, there was no HER2 patient and only 2 TN BC patients in our prospective cohort 1 (**Table S1**). Still, in this dataset, we could detect that TN BC patients exhibited higher proportions of iCAF clusters than LumA BC patients, which accumulated more myCAF clusters (in LumA: iCAF = 43.4%, myCAF= 56.6%; in TN: iCAF = 57.1%, myCAF= 42.9%; P value = 1.29e-64 from Fisher's exact test). Due to the low number of TN BC in our dataset, we sought to address this question by taking advantage of the TCGA database, which contains RNA-Seq data from a high number of LumA and TN BC patients. To this end, we first defined specific signatures of the 5 most abundant CAF-S1 clusters (that represented up to 91% of sequenced CAF-S1 cells) by identifying differentially expressed genes in each cluster compared to the others (**Fig. S1D**). As we also used these signatures for detecting these clusters in melanoma, NSCLC and HNSCC data (see below), we next discarded any gene of these signatures that was also expressed by melanoma, NSCLC and HNSCC cancer cells to avoid any signal from cancer cells and to guarantee a signal strictly specific of CAF-S1 clusters (**Data S2** and **Fig. S1D** for specificity of CAF-S1 cluster signatures). We thus assessed the differential of expression of CAF-S1 cluster-specific signatures between LumA and TN BC subtypes from the TCGA RNA-seq database (https://portal.gdc.cancer.gov/). We confirmed the accumulation of iCAF clusters in TN and myCAF clusters in LumA BC (**Fig. S1E**). Specifically, detox-iCAF and IL-iCAF showed higher expression in TN compared to Lum BC, while ecm-myCAF, TGFβ-myCAF and wound-myCAF

expression was higher in LumA BC than in other BC subtypes (**Fig. S1E**), this increase in iCAF content in TN BC being consistent with the reported presence of numerous TILs in some TN BC (8). In summary, using scRNA-seq from a large number of FAP^+ CAF-S1 fibroblasts isolated from BC, we detected 8 clusters that exhibit distinct signatures and accumulated differentially in BC subtypes.

CAF-S1 cellular clusters are validated by multicolor flow cytometry in BC

We next aimed at validating CAF-S1 clusters by using multi-color flow cytometry (FACS) on fresh BC samples. By analyzing the percentage of each cluster among CAF-S1 defined by scRNA-seq, we first observed that the 5 first clusters represented up to 91% of total sequenced cells (**Fig. 2A**). We thus decided to focus our FACS analysis on these 5 most abundant clusters and sought to identify surface markers for each cluster. Using pairwise comparisons of CAF-S1 cluster expression profiles, we identified 6 surface markers with commercially available antibodies and designed a gating strategy to identify the 5 most abundant clusters (**Fig. 2B** and **Fig. S2A**). We sought to validate the specificity of these 6 markers in an independent CAF-S1 dataset. To do so, we studied the CAF-S1 scRNA-seq data corresponding to the 8^{th} patient, in which the clusters labels were transferred successfully by the Label Transfer algorithm (as shown **Fig. S1C**). Indeed, the gating strategy relying on these 6 markers and based on 7 BC patients efficiently delineated the 5 most abundant CAF-S1 clusters in the independent dataset (**Fig. S2B)**. By this way, we confirmed that these markers were specific of each CAF-S1 cluster. We thus analyzed fresh BC samples by FACS by applying the following gating strategy: CAF-S1 fibroblasts (isolated as $CD45^-$, $EPCAM^-$, $CD31^-$, $CD235a^-$, FAP^{High} $CD29^{Med}$) were first separated based on ANTXR1 protein level that distinguished myCAF ($ANTXR1^+$) from iCAF ($ANTXR1^-$) fibroblasts in BC. $ANTXR1^+$ (myCAF) CAF-S1 clusters 0 (ecm-myCAF), 3 (TGFβ-myCAF) and 4 (wound-myCAF) were next distinguished according to SDC1, LAMP5 and CD9 protein levels. $ANTXR1^+$ $SDC1^+$ $LAMP5^-$ were defined as cluster 0 (ecm-myCAF), $ANTXR1^+$ $LAMP5^+$ $SDC1^{+/-}$ as cluster 3 (TGFβ-myCAF), and $ANTXR1^+$ $SDC1^-$ $LAMP5^-$ $CD9^+$ as cluster 4 (wound-myCAF) (**Fig. 2C)**. $ANTXR1^-$ (iCAF) CAF-S1 clusters 1 (detox-iCAF) and 2 (IL-iCAF)

were separated using GPC3 and DLK1 markers. ANTXR1^{-} GPC3^{+} DLK1$^{+/-}$ were defined as cluster 1 (detox-iCAF); ANTXR1^{-} GPC3^{-} DLK1^{+} as cluster 2 (IL-iCAF) (**Fig. 2C**). ANTXR1^{+} CAF-S1 cells that were negative for LAMP5, SDC1 and CD9 and ANTXR1^{-} GPC3^{-} DLK1^{-} cells were pooled and referred to as "other cluster". By applying this gating strategy on 44 fresh samples (prospective cohort 2, **Table S1)**, we validated the existence of these 5 most abundant clusters in BC (**Fig. 2D**). The percentage of each cluster among CAF-S1 cells defined by FACS confirmed the single-cell results, including clear heterogeneity among CAF-S1 fibroblasts and ecm-myCAF as the most abundant population in the majority of patients (**Fig. 2D**). We next analyzed if there was any correlation between the respective proportions of these 5 CAF-S1 clusters across patients (see correlation matrix **Fig. 2E**, and detailed correlation plots on the right). We detected that the relative abundances of ecm-myCAF and TGFβ-myCAF (both myCAF) were correlated together, as well as those of detox-iCAF and IL-iCAF (both iCAF) (**Fig. 2E,** detailed correlation plots on the right). Conversely, the proportions of ecm-myCAF and TGFβ-myCAF were anti-correlated with the ones of detox-iCAF and IL-iCAF (**Fig. 2E**). In addition, the wound-myCAF was negatively correlated with detox-iCAF, IL-iCAF but also with ecm-myCAF (**Fig. 2E,** detailed correlation plots at bottom), suggesting that these different CAF-S1 clusters could accumulate differentially in BC but in a coordinated manner.

CAF-S1 cellular clusters are identified across cancer types

We next sought to test the existence of CAF-S1 cellular clusters in other cancer types. To do so, we analyzed publicly available scRNA-seq data from head and neck squamous cell carcinoma (HNSCC) (30) and non-small cell lung cancer (NSCLC) (31), since these two studies had isolated enough CAF to investigate clusters. These published studies, included 18 HNSCC patients, of which 5 matched pairs of primary tumors and lymph nodes metastases, for a total of 5902 total cells analyzed (30). Moreover, in the NSCLC cohort, more than 52 000 total cells were collected from 5 different patients (31). In these two studies, 1422 cells and 1465 cells were annotated as CAF in HNSCC and NSCLC cohorts, respectively (30,31). To pursue the analysis strictly on CAF-S1 fibroblasts, CAF-S1 were distinguished from CAF-S4 based on the expression

of FAP and MCAM, two markers regulated at RNA levels in CAF-S1 (FAP^{High} $MCAM^{Low}$) and CAF-S4 (FAP^{Low} $MCAM^{High}$) respectively (8) (**Fig. S2C**). As a result, 603 CAF-S1 cells in HNSCC and 959 in NSCLC were further analyzed. We compared the similarity between CAF-S1 cells from distinct cancer types by mixing the referent (BC) and target (HNSCC or NSCLC) datasets. Data integration was done using "anchor" correspondences across single-cells from different datasets on the basis of the similarity of their expression profiles, as described in (28) (**Fig. 3**). We used CAF-S1 cluster-specific signatures defined by differentially expressed genes in each cluster compared to the others (**Data S2** and **Fig. S1D**). Remarkably, we found systematic correspondences between CAF-S1 clusters from BC with CAF-S1 clusters from either HNSCC (**Fig. 3A**) or NSCLC (**Fig. 3B**). Visualization of the clusters using specific signatures confirmed that we could detect the 5 most abundant clusters in HNSCC and NSCLC (**Fig. 3A, B**). Hence, we could confirm the existence of the 5 most abundant CAF-S1 clusters in HNSCC and NSCLC, highlighting their relevance in other cancers.

Immunosuppressive environment correlates with specific CAF-S1 clusters

As we showed that CAF-S1 fibroblasts exert immunosuppression in breast and ovarian cancers (8,10), we next investigated whether this function could be exerted by all CAF-S1 clusters or restricted to specific ones (**Fig. 4**). We first tested if we could detect correlations between the content of CAF-S1 clusters and immune cells. To this end, fresh BC samples (prospective cohort 2, **Table S1**) were characterized both in terms of CAF-S1 cluster content (as shown **Fig. 2**) and immune cell infiltration, including $CD4^+$, $CD8^+$ T lymphocytes and natural killer (NK) cells (**Fig. S3A-C**). We tested associations between stromal and immune cells and analyzed variables exhibiting at least one significant correlation with another variable (**Fig. 4A**). The correlation matrix obtained by unsupervised hierarchical clustering highlighted that ecm-myCAF and TGFβ-myCAF are clustered together on the one side, detox-iCAF and IL-iCAF clusters on the other, while the wound-myCAF cluster was quite isolated (**Fig. 4A**), suggesting that these different clusters interact differentially with T cells. Interestingly, we found that ecm-myCAF, TGFβ-myCAF and wound-myCAF showed specific associations with T lymphocytes (**Fig. 4A**).

Indeed, we first observed that the proportion of ecm-myCAF among CAF-S1 fibroblasts was significantly correlated with $CD45^+$ hematopoietic cells infiltration (**Fig. S3D**). More specifically, the abundance of ecm-myCAF was correlated with infiltration of PD-1^+, CTLA-4^+ and $TIGIT^+$ $CD4^+$ T lymphocytes, but anti-correlated with $CD8^+$ T lymphocytes (**Fig. 4A**, right, red square). Likewise, although the content in TGFβ-myCAF did not show any global association with $CD45^+$ hematopoietic cells, its abundance was positively correlated with infiltration by CTLA-4^+ $CD4^+$ T lymphocytes and negatively correlated with $CD8^+$ T lymphocytes (**Fig. 4A,** right, green square). Thus, these data indicate that the abundance of ecm-myCAF and TGFβ-myCAF is associated with an immunosuppressive environment enriched in Tregs. In contrast to ecm-myCAF and TGFβ-myCAF clusters, the abundance of detox-iCAF and IL-iCAF was correlated with $CD8^+$ T cell infiltration (**Fig. 4A**, right, yellow and green squares). The wound-myCAF cluster was globally correlated with T lymphocytes among $CD45^+$ cells (**Fig. S3D**) and anti-correlated with CTLA-4^+, $TIGIT^+$, PD-1^+ and $NKG2A^+$ $CD4^+$ T lymphocytes (**Fig. 4A**, bottom, blue square and **Fig. S3D**). The enrichment in wound-myCAF was also anti-correlated with CTLA-4^+ $CD8^+$, TIGIT $CD8^+$, $CD244^+$ $CD8^+$, $CD244^+$ NK (**Fig. 4A**, bottom, blue square), markers of exhaustion, suggesting a global association of this cluster with high T lymphocyte infiltration and immuno-protective environment.

To validate these data in an independent and large cohort of BC patients, we next tested the association between CAF-S1 clusters and T cell signatures in the publicly-available TCGA database. RNA-seq data from TCGA database enabled us to confirm that the expression of ecm-myCAF and TGFβ-myCAF clusters was positively correlated with the one of FOXP3 (**Fig. 4B**), one of the main Treg markers. In addition, while wound-myCAF showed no real association with FOXP3, detox-iCAF and IL-iCAF clusters were negatively correlated with FOXP3 (**Fig. 4B**). In agreement with these data, we observed a positive correlation between T cell cytolytic index, as defined in (32), and detox-iCAF and IL-iCAF clusters, but not with ecm-myCAF, TGFβ-myCAF or wound-myCAF (**Fig. 4C**). To summarize, while detox-iCAF and IL-iCAF are correlated with immunocompetent environment, both ecm-myCAF and TGFβ-

myCAF are associated with an immunosuppressive environment, poor in $CD8^+$ T lymphocytes and enriched in $CD4^+$ T lymphocytes expressing high levels of immune checkpoints, including PD-1, CTLA-4.

Positive feedback loop between ecm-myCAF and TGFβ-myCAF with PD-1^+ and CTLA-4^+ Tregs

As described above, we observed that the abundance of ecm-myCAF and TGFβ-myCAF, but not detox-iCAF and IL-iCAF, is correlated with that of PD-1^+ and/or CTLA-4^+ $CD4^+$ T lymphocytes in BC. We investigated the role of CAF-S1 clusters in generating a $CD4^+$ $CD25^+$-enriched immunosuppressive environment. We therefore established primary cultures of CAF-S1 clusters in order to perform *in vitro* functional assays. Although we did not achieve to establish every CAF-S1 clusters in culture, we succeeded at isolating ecm-myCAF and iCAF clusters by applying two distinct methods, i.e. (1) by leaving CAF-S1 fibroblasts directly escaping and spreading from BC samples seeded in plastic dishes, and (2) by sorting FAP^{High} $CD29^{Med}$ cells by FACS and expanding them in culture in plastic dishes. After expansion during few weeks, we compared the identity of these different cells in the same culture conditions, i. e. those compatible with co-culture with $CD4^+$ $CD25^+$ T lymphocytes for performing functional assays (see below). We observed that CAF-S1 obtained by spreading expressed high levels of myCAF genes, while CAF-S1 isolated by sorting exhibited high expression of iCAF genes (**Fig. 5A**). We thus applied the cluster-specific signatures established from scRNA-seq data (**Data S2** and **Fig. S1D**) and found that spread CAF-S1 fibroblasts were enriched in ecm-myCAF, while sorted CAF-S1 were enriched in detox-iCAF, IL-iCAF and IFNγ-iCAF clusters (**Fig. 5A**, see also Methods' section #*RNA sequencing of CAF-S1 primary cell lines isolated from BC*). Thus, although we did not obtain all pure CAF-S1 clusters *in vitro*, we succeeded in generating ecm-myCAF and iCAF using these two methods that enabled us to compare the respective properties of these clusters. We have previously demonstrated that the global CAF-S1 subpopulation has no direct effect on $CD4^+$ $CD25^-$ T cells but increases the proportion of $FOXP3^+$ Tregs among $CD4^+$ $CD25^+$ T lymphocytes (8,10). As the content in ecm-myCAF and TGFβ-myCAF in BC was associated

with a $CD4^+$-enriched immunosuppressive micro-environment while iCAF clusters were not, we compared the function of these myCAF and iCAF clusters on $CD4^+$ $CD25^+$ T cells using functional assays, as previously performed in (8,10).

At first, we tested the impact of myCAF and iCAF clusters on the content of $CD4^+$ $CD25^+$ $FOXP3^+$ T lymphocytes *in vitro* (**Fig. 5B**). ecm-myCAF increased the percentage of $FOXP3^+$ T cells among the $CD4^+$ $CD25^+$ population and enhanced the FOXP3 protein level in these T cells (**Fig. 5B**). In contrast, iCAF clusters had no impact on either the percentage of $CD4^+$ $CD25^+$ $FOXP3^+$ T lymphocytes or on FOXP3 protein levels (**Fig. 5B**). We also tested the impact of culture on the identity and immunosuppressive activity of normal fibroblasts. Fibroblasts isolated upon spreading from healthy tissues were $FAP^{Neg\text{-}Low}$ and devoid of immunosuppressive activity at early time point, but became $FAP^{Pos\text{-}High}$ and immunosuppressive at later passages (**Fig. S4A, B**), suggesting that the maintenance at long term of CAF on plastic dishes may activate them. Based on the ability of ecm-myCAF to increase $CD4^+$ $CD25^+$ $FOXP3^+$ T lymphocytes, we next compared the capacity of CAF-S1 clusters to modulate the proportion of $PD\text{-}1^+$, $CTLA\text{-}4^+$, $TIGIT^+$, $TIM3^+$ and $LAG3^+$ on $CD4^+$ $CD25^+$ $FOXP3^+$ T lymphocytes, considering both percentage of positive cells and surface protein levels of these immune checkpoints (**Fig. 5C-G**). ecm-myCAF significantly increased both percentage of $PD\text{-}1^+$ and $CTLA\text{-}4^+$ $CD4^+$ $CD25^+$ $FOXP3^+$ T lymphocytes and immune checkpoint levels at their surface (**Fig. 5C, D**). In contrast to ecm-myCAF, iCAF clusters neither affected the percentage of $PD\text{-}1^+$ and $CTLA\text{-}4^+$ T cells nor CTLA-4 protein levels (**Fig. 5C, D**). Furthermore, although iCAF clusters increased PD-1 protein levels, this effect was at lower efficiency than ecm-myCAF. Both myCAF and iCAF clusters increased the proportion of $CD4^+$ $CD25^+$ $FOXP3^+$ $TIGIT^+$ cells (**Fig. 5E**), while they had no effect on $TIM3^+$ and $LAG3^+$ T cells (**Fig. 5F, G**). Hence, in agreement with the correlations observed in BC between ecm-myCAF and $PD\text{-}1^+$ and $CTLA\text{-}4^+$ $CD4^+$ T lymphocytes, we show here that CAF-S1 from ecm-myCAF have a direct function on Tregs by enhancing PD-1 and CTLA-4 immune checkpoint levels at the surface of $CD4^+$ $CD25^+$ $FOXP3^+$ T lymphocytes, while iCAF clusters have no or minimal effect on these cells. Finally, we observed that the up-regulation of immune checkpoints at the

surface of $CD4^+$ $CD25^+$ T cells upon co-culture with ecm-myCAF was also detected intracellularly (**Fig. S4C**), suggesting that ecm-myCAF increased the total protein levels in T cells. Moreover, we found that expression of FOXP3, CTLA-4, and TIGIT in $CD4^+$ $CD25^+$ T cells were also up-regulated at mRNA levels following co-culture with ecm-myCAF (**Fig. S4D**), PD-1 RNA being almost not detected in T cells *in vitro*. Furthermore, we observed that mRNA levels of NFAT and STAT family members were also elevated in $CD4^+$ $CD25^+$ T lymphocytes upon co-culture with ecm-myCAF (**Fig. S4E**). As NFAT and STAT are well-known transcriptional regulators of immune checkpoints in T cells, these data indicate that ecm-myCAF promotes up-regulation of immune checkpoints at RNA levels in $CD4^+$ $CD25^+$ T lymphocytes, potentially through the activation of NFAT/STAT-signaling pathways.

Considering the impact of CAF-S1 clusters on Tregs, we next wondered whether T lymphocytes could in turn modulate CAF-S1 cluster identity. We thus evaluated if co-culturing $CD4^+$ $CD25^+$ T lymphocytes had any impact on the marker cluster levels at the surface of CAF-S1 fibroblasts (**Fig. 5H**). Upon co-culture, to avoid any contamination by T cells, we isolated CAF-S1 by FACS and analyzed cluster markers expressed at their surface. We observed that the co-culture of $CD4^+$ $CD25^+$ T cells significantly increased the expression of the TGFβ-myCAF specific marker LAMP5, at the surface of ecm-myCAF fibroblasts (**Fig. 5H**), thereby suggesting that the content in TGFβ-myCAF increases upon co-culture with $CD4^+$ $CD25^+$ T lymphocytes. This effect was only detected in myCAF and not in iCAF fibroblasts (**Fig. 5H**), as expected considering that TGFβ-myCAF and ecm-myCAF CAF-S1 fibroblasts belong to the myCAF subgroup (**Fig. 1E,F**). Consistent with this observation, ANTXR1 protein level also showed a trend to increase (although without reaching significance) in ecm-myCAF fibroblasts upon co-culture with $CD4^+$ $CD25^+$ T cells, while it remained strictly unchanged and low in iCAF cells (**Fig. 5H**). Quite surprisingly, DLK1, marker of IL-iCAF, also increased upon co-culture, suggesting a potential plasticity between ecm-myCAF and IL-iCAF. In contrast, the other markers did not show any significant variation upon co-culture and remained either high (SDC1) or low (GPC3 and CD9), as expected based on respective cluster identity (**Fig. 5H**).

These observations suggest that CD4$^+$ CD25$^+$ T lymphocytes might promote conversion of ecm-myCAF (ANTXR1$^+$ SDC1$^+$ LAMP5$^-$ CD9$^{+/-}$) into TGFβ-myCAF (ANTXR1$^+$ LAMP5$^+$ SDC1$^{+/-}$ CD9$^{+/-}$), both clusters being myCAF. Taken as a whole, we found that ecm-myCAF can directly impact on PD-1 and CTLA-4 protein levels at the surface of FOXP3$^+$ T lymphocytes. Reciprocally, Tregs can promote the conversion of ecm-myCAF into TGFβ-myCAF, thereby underlying a positive feedback loop between these two clusters and CD4$^+$ CD25$^+$ PD-1$^+$ or CTLA-4$^+$ T cells) that could account for the positive correlations we observed in BC.

ecm-myCAF and TGFβ-myCAF are associated with primary resistance to immunotherapy

Given the direct effect of specific CAF-S1 clusters on PD-1 and CTLA-4 protein levels on Tregs, we next wondered whether some CAF-S1 clusters could be associated with immunotherapy resistance. As we did not have access to data from BC treated by immunotherapy, we took advantage of publicly available data from metastatic melanoma patients treated with anti-PD-1 (Pembrolizumab) therapy (33), which has revolutionized melanoma treatment. As defined in the aforementioned study, we considered patients as “non-responders” to anti-PD-1 if they showed progressive disease, and as “responders” in case of complete or partial response. By performing gene set enrichment analysis, we first observed that, at time of diagnosis, expression of CAF-S1-specific genes, but not of normal fibroblast content, was significantly enriched in tumors from non-responder patients (**Fig. 6A**). Using CAF-S1 cluster-specific signatures (**Data S2**), we observed that ecm-myCAF, TGFβ-myCAF and wound-myCAF gene expression was enriched in non-responders compared to responders, while detox-iCAF, IL-iCAF and IFNγ-iCAF clusters were not (**Fig. 6B**). We next compared the content in each CAF-S1 cluster in responders *versus* non-responders. We confirmed that ecm-myCAF, TGFβ-myCAF and wound-myCAF expression was significantly higher in non-responders than in responders, while detox-iCAF and IFNγ-iCAF expression was similar between the two subgroups of patients (**Fig. 6C**). Moreover, neither the normal fibroblast content, nor the cytolytic index, defined in (32), was different between responders and non-responders (**Fig. 6D, E**). In agreement with these observations, the

reciprocal analysis (i.e. determining the number of responders and non-responders according to low- or high-CAF-S1 cluster expression) confirmed that the number of non-responder patients was significantly associated with tumors showing high expression of ecm-myCAF, TGFβ-myCAF or wound-myCAF at diagnostic, while the other CAF-S1 clusters, the general CAF content or the cytolytic index were not informative on patient response to immunotherapy (**Fig. 6F-H**). Together, these data show that 3 specific CAF-S1 clusters (ecm-myCAF, TGFβ-myCAF and wound-myCAF) are indicative at diagnosis of anti-PD-1 response in metastatic melanoma patients, while the other CAF-S1 clusters (detox-iCAF, IL-iCAF and IFNγ-iCAF), the total CAF content or the cytolytic index are not. Finally, we sought to validate the impact of CAF-S1 clusters, in particular ecm-myCAF, TGFβ-myCAF and wound-myCAF, on primary immunotherapy resistance in a series of metastatic NSCLC patients, another recently established clinical indication for immunotherapy (here treated in second- or third-line setting with Nivolumab, see **Table S2** for detailed description of the NSCLC cohort 4). Similar to melanoma, we validated that CAF-S1 signature, evaluated in tumor specimens sampled at diagnosis, was significantly enriched in non-responder patients (**Fig. 6I**). In contrast, the normal fibroblast content was higher in responders than in non-responders, suggesting that CAF-S1 was significantly enriched in non-responders (**Fig. 6I**). Importantly, we confirmed that ecm-myCAF, TGFβ-myCAF and wound-myCAF were associated with non-responder NSCLC patients, as opposed to detox-iCAF, IL-iCAF and IFNγ-iCAF clusters (**Fig. 6J**). In conclusion, in contrast to detox-iCAF, IL-iCAF and IFNγ-iCAF clusters, the abundance of ecm-myCAF and TGFβ-myCAF at diagnosis is associated with resistance to immunotherapy in both melanoma and NSCLC, consistent with their capacity to increase PD-1^{+} and CTLA-4^{+} protein levels in Tregs.

DISCUSSION

By performing scRNA-seq on more than 19 000 CAF-S1 fibroblasts from BC patients, we identified 8 cellular clusters within the CAF-S1 immunosuppressive subset in human BC. We validated the existence of the 5 most abundant clusters by FACS using specific surface markers. We dissected the most prominent pathways and gene specific signatures characterizing each CAF-S1 cluster, as followed: ECM (cluster 0/ecm-myCAF), detoxification (cluster 1/detox-iCAF), response to stimuli (cluster 2/IL-iCAF), TGFβ (cluster 3/TGFβ-myCAF), wound-healing (cluster 4/wound-myCAF), IFNγ and cytokines (cluster 5/IFNγ-iCAF), IFNα/β (cluster 6/IFNαβ-iCAF) and acto-myosin (cluster 7/acto-myCAF). We took advantage of these specific signatures to show that the different CAF-S1 clusters exhibit a distinct accumulation in BC subtypes and to confirm their existence in publicly available datasets from HNSCC and NSCLC, thereby underlying the relevance of our findings. Among the 5 most abundant clusters, ecm-myCAF and TGFβ-myCAF are specifically associated with an immunosuppressive environment, as their abundance correlate with the one of PD-1$^+$ and/or CTLA-4$^+$ CD4$^+$ T cells. Importantly, ecm-myCAF and TGFβ-myCAF are enriched at time of diagnosis in samples from melanoma and NSCLC patients who did not respond to immunotherapies. Consistent with these observations, we demonstrated that ecm-myCAF are able to increase the expression of PD-1 and CTLA-4 at the surface of FOXP3$^+$ Tregs. Reciprocally, CD4$^+$ CD25$^+$ T lymphocytes promote the conversion of ecm-myCAF into TGFβ-myCAF fibroblasts. These data therefore demonstrate an interesting reciprocal cross-talk between specific ecm-myCAF and TGFβ-myCAF with CD4$^+$ CD25$^+$ T lymphocytes, that could promote immunosuppression and be involved in resistance to immunotherapies.

Heterogeneity in cellular composition represents a major challenge in modern oncology. In recent years, scRNA-seq appeared as a revolutionary technic for addressing intra-tumor cellular complexity (27,30,34-44). In addition to cancer cells, previous studies have provided the first comprehensive catalogs of normal cells that compose the tumor micro-environment, most of

these studies being focused on immune cell heterogeneity (31,45-51). Recently, we and others have identified different CAF subsets in various adenocarcinomas, including two subpopulations defined either by adhesion/wound-healing (CAF-S1) or peri-vascular/contractile (CAF-S4) signatures (7-16). The first single cell data on CAF from human cancers and mouse models confirmed the existence of ECM-rich (CAF-S1) and contractile (CAF-S4) sub-populations (16,24,26,29,38), indicating that CAF-S1 and CAF-S4 can be detected in distinct cancer types and across species. Here, we go a step further by analyzing a large number of immunosuppressive CAF-S1 cells, reaching -to our knowledge- an unprecedented resolution of this subpopulation. Unbiased methods enabled us to identify specific gene signatures that distinguish different CAF-S1 cellular clusters, which highlights the diversity of this particular CAF subpopulation within cancers. We confirmed the identification of two CAF-S1 myCAF and iCAF fibroblast subtypes, previously identified in pancreatic cancers (7,16,26,29). Our analysis increases CAF-S1 cellular resolution by showing that both myCAF and iCAF fibroblasts can be themselves further subdivided into different cellular clusters. CAF-S1 from the clusters 1 and 2 (detox-iCAF and IL-iCAF) are characterized by detoxification and inflammatory signaling, and by response to interleukin and TNF pathways, respectively. CAF-S1 from cluster 5 (IFNγ-iCAF) are enriched in IFNγ signature and exhibit high expression of CD74, a marker of the antigen-presenting CAF (apCAF) subset recently identified in pancreatic cancers (16), suggesting cluster 5/IFNγ-iCAF might be the “apCAF” counterpart in BC. Among myCAF, CAF-S1 cluster 0 is enriched in genes encoding ECM and ECM remodeling proteins and was referred to as “ecm-myCAF”. Interestingly, ecm-myCAF specific signature contains the LRRC15 gene that has been recently identified in pancreatic cancer (29). In addition, myCAF from cluster 3 are specified by TGFβ-signaling pathway and was defined as “TGFβ-myCAF”. Importantly, we confirmed the existence of the 5 most abundant clusters by using flow cytometry in BC. We also detected these distinct CAF-S1 cellular clusters in HNSCC and NSCLC, demonstrating the relevance of our findings across cancer types. Additionally, we unraveled that the CAF-S1 clusters exhibit a distinct accumulation in the different BC subtypes,

with the detox-iCAF and IL-iCAF being predominant in TN BC, consistent with the possible presence of numerous TILs in this specific BC subtype (8).

Cancer immunotherapy has emerged as an effective therapy in oncology. However, despite encouraging results, many advanced cancer patients do not respond to immune checkpoint inhibitors, and little is known about the mechanisms of primary resistance. Identification of biomarkers that may reliably discriminate responder and non-responder patients before initiating therapy is hence needed to select patients who are likely to benefit from immuno-oncology drugs. Here, we show that several CAF-S1 clusters could actually contribute to primary resistance to immunotherapy. In addition to well-known factors involved in immunotherapy resistance, such as lack of antigen presentation, tumor immunogenicity deficiency, T cell exclusion or defective tumor cell response to IFNγ (52-55), we identify here specific CAF-S1 cellular clusters as new key players in primary resistance to immunotherapy. We demonstrate that the abundance of ecm-myCAF and TGFβ-myCAF in tumors is anti-correlated with $CD8^+$ T cells infiltration, but correlated with PD-1^+ and CTLA-4^+ $CD4^+$ T cell content in BC. Moreover, our results support the existence of a reciprocal crosstalk between the ecm-myCAF and TGFβ-myCAF clusters, on the one hand, and Tregs on the other, which could reinforce the role of these clusters in immunotherapy resistance. Indeed, ecm-myCAF enhance the expression of PD-1 and CTLA-4 at the surface of CD4+ CD25+ FOXP3+ T lymphocytes, thereby leading to a global increase in PD-1^+ and CTLA-4^+ Tregs. Reciprocally, Tregs tend to promote the conversion of CAF-S1 fibroblasts from ecm-myCAF to TGFβ-myCAF. This reciprocal cross-talk explains -at least in part- the enrichment in ecm-myCAF and TGFβ-myCAF in tumors that are highly infiltrated by Tregs. It also provides some clues for the link of ecm-myCAF and TGFβ-myCAF with immunotherapy resistance, in agreement with recent findings on *LRCC15* (29), which is one of the gene of the ecm-myCAF signature. In contrast to ecm-myCAF and TGFβ-myCAF, wound-myCAF are not associated with an immunosuppressive environment, but correlated with a high global infiltration by T lymphocytes. Hence, as the wound-myCAF cluster is enriched in tumors from patients who do

not respond to immunotherapy, it might serve as a new surrogate marker of primary resistance to immunotherapies in highly infiltrated tumors, which are usually sensitive to this type of treatment. Still, the mechanistic explanation for the role of wound-myCAF in this paradoxical observation remains elusive. As expected if we consider that IFNγ-iCAF are reminiscent of the antigen-presenting CAF "apCAF" subset recently identified (16), this cluster is not indicative of immunotherapy resistance. Taken as a whole, these findings suggest that -although important- infiltration by $CD8^+$ and Tregs might not be sufficient on their own for defining non-responder patients. Thus, assessing the content in specific CAF-S1 clusters in tumors at time of diagnosis could provide an additive value for predicting primary resistance to immune checkpoint inhibitors.

ecm-myCAF and TGFβ-myCAF are characterized by signatures of genes involved in collagen synthesis and ECM organization and response to TGFβ stimulus, respectively. TGFβ was shown to attenuate anti-PD-L1 response by contributing to T cell exclusion, while TGFβ inhibition was shown to unleash potent cytotoxic T cell response against tumor cells (11,19,56-58). Consistent with these observations, TGFβ-myCAF express high levels of TGFβ1 and TGFβ3. In addition, stromal- and mesenchymal-gene expression have been previously related to resistance to anti-PD-1/PD-L1 blockade in melanoma, urothelial and colorectal cancers (29,38,58-60). The dense networks of CAF-secreted collagen fibers in tumor nests have been shown to constitute a physical barrier that prevents T cells to reach tumor bed (61). CAF-S1 fibroblasts also exert an active function in immunosuppression by increasing attraction, survival and activation of $FOXP3^+$ T lymphocytes (8,10). Here, we go a step further by showing that ecm-myCAF are able to stimulate PD-1 and CTLA-4 protein levels at the surface of $FOXP3^+$ T cells, which might influence anti-PD1 immunotherapy effectiveness. The increase in CTLA-4 expression at the surface of Tregs could also be a mechanism to bypass PD-1 blockade and to contribute to immune exhaustion persistence. Such increased CTLA-4 expression by Tregs has been suspected to be the biological basis for the additive effect of anti-CTLA-4 antibodies when used in combination with anti-PD-1 checkpoint inhibitors. This combination has recently been shown to improve overall survival, as compared with chemotherapy, in first-line setting of metastatic NSCLC

patients (62). These data thus support the development of strategies combining PD-1 and/or CTLA-4 blockade with therapies targeting CAF-S1 clusters components to overcome primary resistance to immune checkpoint blockade.

ACKNOWLEDGEMENTS

We thank Drs. Virginie Mieulet and Josh Waterfall for critical reading of the manuscript, as well as Drs. Emanuela Romano, Itay Tirosh and the GDR 3697 Micronit for fruitful discussions. We are grateful to Charlotte Martinat, from the Diagnostic and Theragnostic Department, Arnaud Meng from the "Stress and Cancer" lab (U830); as well as Renaud Leclere and André Nicolas from the experimental pathology platform at the Institut Curie for help and advices. We are also grateful to Celine Namour and Zohra Brouk for clinical data management at the Early phase Clinical Research Unit, Thoracic Oncology Department, CIC1425/CLIP$_2$ Paris-Nord, from Bichat Hospital (Assistance Publique-Hôpitaux de Paris). **Funding:** Y.K., C.B. G.G. and HR.H. were supported by the Institut National du Cancer, INCa (INCa-DGOS-9963; INCa-11692), SIRIC (INCa-DGOS-4654), the Medical Research Foundation (FRM) and the Foundation ARC (AAP SIGN'IT 2019). A.Z. is partly supported by the Agence Nationale de la recherche (ANR-19-P3IA-0001). The NGS platform was supported by grant from France Génomique Consortium (ANR-10-INBS-09-08). The experimental work was supported by grants from the Ligue Nationale Contre le Cancer (*Labelisation*), Inserm (PC201317), Institut Curie (Incentive and Cooperative Program Tumor Micro-environment PIC TME/T-MEGA, PIC3i CAFi), Bristol-Myers Squibb Foundation (call 2018 for Research in Immuno-oncology), ICGex (ANR-10-EQPX-03), SIRIC (INCa-DGOS-4654), INCa (STROMAE INCa-DGOS-9963, CaLYS INCa-11692, INCa-DGOS-Inserm-12554). F.M-G acknowledges the french Pink Ribbon Association « Le cancer du sein, Parlons-en » and the Simone and Cino del Duca Foundation for attribution of their "Grand Prix". F.M-G is very grateful to all her funders for providing support throughout the years.

AUTHOR CONTRIBUTIONS

F.M-G. conceived the project and designed the experiments. Y.K. and C.B. performed bioinformatic and statistical analyses. F.P. and HR.H. isolated CAF-S1 single cells from BC and performed experiments. HR.H., G.G. and B.B. performed FACS and *in vitro* experiments. S.L. and S.B. performed single cell RNA sequencing. L.A. and A.Z. provided knowledge on

scRNA-seq bioinformatic analyses and K.T. on CAF signatures. A.V-S. provided human samples from the Curie cohorts and expertise in pathology analysis. G.Z. and A.G. built the NSCLC cohort and provided pathological and clinical information. F.M-G. supervised the entire project and wrote the paper with Y.K. and HR.H., with suggestions from all authors.

DATA AVAILABILITY

scRNA-seq data sorted from BC samples are available on European Genome-Phenome Archive platform (https://ega-archive.org) under accession number: EGAS00001004030. RNA-seq data from iCAF (sorted) and ecm-myCAF (spread) CAF-S1 fibroblasts maintained in culture are available on EGA platform under accession number: EGAS00001004031. RNA-seq data from NSCLC samples are available on EGA platform under accession number: EGAS00001004032.

METHODS

Cohorts of patients

BC patients: The study developed here is based on samples taken from surgical residues, available after histopathological analyses, and not required for diagnosis. There is no interference with clinical practice. Analysis of primary tumor samples was performed in accordance with the relevant national law and with recognized ethical guidelines (Declaration of Helsinki), on the protection of people taking part in biomedical research. All patients hospitalized at Institut Curie (BC patients) received a welcome booklet explaining that their samples may be used for research purposes. All patients included in our study were thus informed by their referring oncologist that biological samples collected through standard clinical practice could be used for research purposes and they gave their verbal informed consent. In case of patient refusal, that could be either orally expressed or written, residual tumor samples were not included in our study. Human experimental procedures for analyses of tumor micro-environment by F. Mechta-Grigoriou's lab were approved by the Institutional Review Board and Ethics committee of the Institut Curie Hospital group (approval February 12th, 2014) and CNIL (Commission Nationale de l'informatique et des Libertés) (Nº approval: 1674356 delivered March 30th, 2013). The 'Biological Resource Centre' (BRC) is part of to the Pathology Department, in the Diagnostic and Theragnostic Medicine Department headed by Dr. A. Vincent-Salomon. BRC is authorized to store and manage human biological samples according to French legislation. The BRC has declared defined sample collections that are continuously incremented as and when patient consent forms are obtained (declaration number # DC-2008-57). The BRC follows all currently required national and international ethical rules, including the declaration of Helsinki. The BRC has also been accredited with the AFNOR NFS-96-900 quality label (renewed and currently valid until 2021). All samples are pseudo-anonymous when they arrive from the BRC in the lab. In addition, the BRC collections have been declared to the CNIL (Approval n° 1487390 delivered February 28th, 2011). Luminal (Lum) tumors were defined by positive immunostaining for ER (Estrogen receptor) and/or PR

(Progesterone receptor). The cut-off used to define hormone receptor positivity was 10% of stained cells. Ki67 (proliferation) score further distinguishes Lum A from Lum B tumors (below 15%: Lum A, above: Lum B). HER2-amplified carcinomas have been defined according to ERBB2 immunostaining using ASCO's guideline. TN immunophenotype was defined as follows: ER^-PR^- $ERBB2^-$ with the expression of at least one of the following markers: $KRT5/6^+$ or $EGF\text{-}R^+$.

NSCLC patients: NSCLC samples were from the routine diagnostic samples stored in the Pathology Department of Bichat Hospital, from patients treated by immuno-oncology drugs in the Thoracic Oncology Department of Bichat hospital headed by Pr. G. Zalcman, MD. The de-identified clinical data were part of the thoracic oncology database of lung cancer patients from the Clinical Investigation Centre (co-headed by Pr. G. Zalcman) CIC-1425/$CLIP_2$ of Bichat Hospital (Regional Health Agency authorization #17-1381), in accordance with French regulatory rules for observational clinical research. Patients received checkpoint inhibitors, after progression upon chemotherapy-based 1^{st} or 2^{nd} line, according to the registration of immuno-oncology drugs. During the current study period, the anti-PD-1 Nivolumab monoclonal antibody represented the most frequent drug used in such setting. Efficacy of immuno-oncology treatment was assessed every 8 to 12 weeks by whole body CT-scan, by a weekly multidisciplinary tumor board, including thoracic specialized radiologists, thoracic oncologists and pulmonologists, according to RECIST v.1.1 criteria, defining objective responders (OR), patients with stable disease (SD) and patients showing tumor progression (Progr) with 20% of more increase in their tumor volume without any clinical benefit. The best response status observed at 4 months was used in the current study. SD patients, for whom immuno-oncology drug was given more than 6 months because of a clinical benefit at 4 month evaluation (n= 3), without any criteria for progressive disease (then long-lasting SD), were included in the group of responder patients in the current study. Date of the CT-scan assessed progression was recorded. Some patients showed an early clinical progression that required an early (before eight weeks) CT-scan assessment. In these series, according to the above-criteria. There were 22 responder patients, 48 progressive patients, who received less than 4 months treatment.

Date of progression was retained as the date of CT-scan showing RECIST progression. Date and cause of death, or date of last news with vital status was systematically recorded. Post-progression 2nd or 3rd-line treatments were registered. There was no unbalance according to post-progression treatments. PD-L1 staining was performed and interpreted by A.G., on 4µm paraffin-embedded sections, from diagnosis, pre-treatment biopsy samples, containing at least 200 tumor cells, using Cell Signaling Technology E1L3N commercially available clone, on the Leica Bond platform. All but 5 patients (having less of 200 tumor cells in the remaining pathological block) had PD-L1 immunohistochemistry analysis.

CAF-S1 RNA sequencing at single cell level

Isolation of CAF-S1 from BC: CAF-S1 fibroblasts were isolated from a total of 8 primary BC (surgical residues prior any treatment) (see Table S1 for details on the prospective cohort). 7 BC were initially studied. In addition, another BC sample was added for validating the CAF-S1 clusters by using the Label Transfer algorithm from Seurat R package. CAF-S1 fibroblasts were isolated from BC by using BDFACS ARIA III™ sorter (BD biosciences). Fresh human BC primary tumors were collected directly from the operating room, after surgical specimen's macroscopic examination and selection of areas of interest by a pathologist. Samples were cut into small pieces (around 1 mm^3) and digested in CO_2-independent medium (Gibco #18045-054) supplemented with 150 µg/ml liberase (Roche #05401020001) and DNase I (Roche #11284932001) during 40 minutes (min) at 37°C with shaking (180 rpm). Cells were then filtrated through a 40 µm cell strainer (Fisher Scientific #223635447) and resuspended in PBS+ solution (PBS, Gibco #14190; EDTA 2 mM, Gibco #15575; Human Serum 1 %, BioWest #S4190-100) at a final concentration between 5 x 10^5 and 10^6 cells in 50 µl. To isolate CAF-S1 fibroblasts, we first apply a selection to exclude epithelial ($EPCAM^+$), hematopoietic ($CD45^+$), endothelial ($CD31^+$), and $CD235a^+$ (red blood) cells and next use CAF-S1 markers (FAP and CD29). To do so, cells in suspension were then stained with an antibody mix containing anti-EpCAM-BV605 (BioLegend, #324224), anti-CD31-PECy7 (BioLegend,

#303118), anti-CD45-APC-Cy7 (BD Biosciences, #BD-557833), anti-CD235a-PerCP/Cy5.5 (Biolegend, #349109), anti-CD29-Alexa Fluor 700 (BioLegend, #303020), anti-FAP-APC (primary antibody, R&D Systems, #MAB3715) for flow cytometry cell sorting in order to perform single cell RNA sequencing. All antibodies except FAP were purchased already conjugated with fluorescent dyes. Anti-FAP antibody was conjugated with fluorescent dye Zenon APC Mouse IgG1 labeling kit (ThermoFisher Scientific, #Z25051). Isotype control antibodies for each CAF marker used were: iso-anti-CD29 (BioLegend, #400144) and iso-anti-FAP (primary antibody, R&D Systems, #MAB002).

Cell suspensions were stained immediately after dissociation of BC tumor samples during 15 min at RT with the antibody mix in PBS+ solution. 2.5 µg/ml DAPI (ThermoFisher scientific, #D1306) was added just before flow cytometry sorting. Signals were acquired on the BDFACS ARIA III^{TM} sorter (BD biosciences) for cell sorting. At least 5 x 10^5 events were recorded. Compensations were performed using single staining on anti-mouse IgG and negative control beads (BD biosciences, #552843) for each antibody. Data analysis was performed using FlowJo version X 10.0.7r2. Cells were first gated based on forward (FSC-A) and side (SSC-A) scatters (measuring cell size and granularity, respectively) to exclude debris. Dead cells were excluded based on their positive staining for DAPI. Single cells were next selected based on SSC-A versus SSC-W parameters. Gating included EPCAM$^-$, CD45$^-$, CD31$^-$, CD235a$^-$ cells, to remove epithelial (EPCAM$^+$), hematopoietic (CD45$^+$), endothelial (CD31$^+$) and red blood cells (CD235a$^+$).

Single cell CAF-S1 RNA sequencing: Upon isolation, CAF-S1 cells were directly collected into RNase-free tubes (ThermoFisher Scientific, #AM12450) pre-coated with DMEM (GE Life Sciences, #SH30243.01) supplemented with 10% FBS (Biosera, #1003/500). At least 6 000 cells were collected per sample. In these conditions, cell concentration was checked in control samples and was of 200 000 cells/ml. Single cell capture, lysis, and cDNA library construction were performed using Chromium^{TM} system from 10X Genomics, with the following kits: Chromium^{TM} Single Cell 3' Library & Gel Bead Kit v2 kit (10X Genomics, #120237) and Chromium^{TM} Single Cell A Chip Kits (10X Genomics, #1000009). Generation of Gel beads in

Emulsion (GEM), barcoding, post GEM-RT (Reverse Transcription) cleanup and cDNA Amplification were performed according to manufacturer's instructions. Targeted cell recovery was 3 000 cells per sample to retrieve enough cells, while preserving a low multiplet rate. Cells were loaded accordingly on the Chromium Single cell A chips and 12 cycles were performed for cDNA amplification. cDNA quality and quantity were checked on Agilent 2100 Bioanalyzer using Agilent High Sensitivity DNA kit (Agilent, #5067-4626) and library construction followed according to 10X Genomics protocol. Libraries were next run on the Illumina HiSeq (for patients P5-7) and NovaSeq (for patients P1-4) with a depth of sequencing of 50 000 reads per cell. Processing of raw data, including demultiplexing of raw base call (BCL) files into FASTQ files, alignment, filtering, barcode and Unique Molecular Identifiers (UMI) counting, were performed using 10X Cell Ranger pipeline version 2.1.1. Reads were aligned to Homo sapiens (human) genome assembly GRCh38 (hg38).

scRNA-seq data processing

scRNAseq: Pre-processing of raw data was initially performed using Cell Ranger software pipeline (version 2.1.1). This step included demultiplexing of raw base call (BCL) files into FASTQ files, reads alignment on human genome assembly GRCh38 using STAR and counting of unique molecular identifier (UMI). A first set of 18 805 CAF-S1 cells from 7 BC patients (corresponding to 7 sequencing runs, patients 1 to 7) were analyzed using Seurat R package (version 3.0.0) (63). A second set of 1646 CAF-S1 cells from one BC patient (patient 8) was used for validation (see #*Label Transfer*) and analyzed using the same methodology.

Quality control: As a quality control step, we first filtered out of low-quality cells, empty droplets and multiplet captures based on the distribution of the unique genes detected (non-zero count) in each cell for each patient. Cells with less than 200 genes detected and more than 6000 genes (for patient 1), more than 5000 genes detected (for patients 3, 5 and 6), more than 4500 genes detected (for patients 2, 7 and 8) or more than 4000 genes detected (for patient 4) were excluded. Distribution of cells based on the fraction of expressed mitochondrial genes was also plotted. Cells with fraction of mitochondrial genes higher than 5% were discarded in order

to eliminate dying cells or low-quality cells with extensive mitochondrial contamination. For each patient, the mitochondrial fraction was computed using *PercentageFeatureSet* function from Seurat with argument pattern = "^MT-". Following these QC criteria, 18 296 CAF-S1 cells (patient1= 1825 cells; patient2= 3300 cells; patient3= 2810 cells; patient4= 3153 cells; patient5= 2486 cells; patient6= 3179 cells and patient7= 1543 cells) and 1582 CAF-S1 cells (patient8) were finally conserved in the first and second datasets respectively for downstream analyses.

Normalization and data integration: Integration of the 7 BC scRNA-Seq from the first dataset was done using Seurat functions *FindIntegrationAnchors* and *IntegrateData* after library-size normalization of each cell using *NormalizeData* function with default parameters. 30 dimensions were used for Canonical correlation analysis (CCA), 30 principal components (PCs) were used in the weighting procedure of *IntegrateData* function. Data were scaled using *ScaleData* function and variables 'nUMI' and 'percent.mt' were used for regression. Same parameters were used for the normalization of the second dataset.

Clustering and data visualization: PCA dimensionality reduction was run using default parameters. Number of included components (PCs) was assessed using JackStraw procedure implemented in *JackStraw* and *ScoreJackStraw* functions. 30 PCs were conserved. Graph-based clustering approach was used to cluster the cells from the first dataset using *FindNeighbours (k = 20)* and *FindClusters* functions (res = 0.35). 10 CAF-S1 clusters were obtained at this resolution. For visualization of the data, non-linear dimensional reduction technique UMAP was applied using the *RunUMAP* function from Seurat.

Analysis of differential gene expression and signaling pathways: Genes specifically up-regulated in each of the 10 clusters of the first dataset were identified using pairwise differential analysis. Although the median number of differentially expressed genes in each pairwise combination was 126 genes, 2 combinations gave a very limited number of differentially expressed genes, with only 9 genes between clusters 0 and 5 and 22 genes between clusters 3 and 6. Biological meaning of each cluster was also determined using Metascape tool (http://metascape.org) using all genes significantly up-regulated in each of the 10 initial clusters

(one cluster *versus* all other clusters; function *FindAllMarkers* with following parameters: logfc.threshold = 0.25, test = wilcox for Wilcoxon Rank Sum test). Consistent with pairwise analysis, biological pathways identified for clusters 0/5 on the one hand, and 3/6 on the other hand, were redundant and thus combined. Clusters 0 and 5 were then defined as cluster 0/ecm-myCAF and clusters 3 and 6 as cluster 3/TGFβ-myCAF to finally identify 8 biologically distinct CAF-S1 clusters.

Gene signatures of CAF-S1, CAF-S1 clusters and normal fibroblasts (Data S2): Specific gene signatures of CAF-S1 clusters 0 to 5 were defined by performing a differential analysis (Wilcoxon rank-sum test) between clusters 0 to 5. Differentially expressed genes between clusters (one cluster *versus* all other clusters) with an adjusted P value < 0.05 were selected. As these signatures were used for detecting CAF-S1 clusters in RNA-seq data from single cells and bulk of different cancer types including melanoma, NSCLC and HNSCC, we excluded genes expressed in tumor cells by using scRNA-seq data from tumor cells of melanoma (27), NSCLC (31) and HNSCC (30). We defined genes expressed in tumor cells (and thus excluded from CAF-S1 cluster signatures) if more than 10% of tumor cells show an expression level higher than 1 in any of the aforementioned scRNA-seq data. Details of the data are given in the 1st tab of the **Data S2**. CAF-S1 global signature was initially published in (8) and submitted to the same type of analysis, excluding genes detected in tumor cells, and thus adapted for bulk analysis. The first 100 most significant genes were considered for the CAF-S1-specific signature. The normal fibroblast signature was defined by the genes significantly up-regulated in normal fibroblasts (FAP^{Neg} CD29^{Med} SMA^{Neg}) isolated from healthy juxta-tumor tissues, compared to CAF-S1 fibroblasts isolated from BC. Genes that are expressed in tumor cells were excluded from the signature, following the same strategy as this one described above. Cytolytic index was defined as the geometric mean of granzyme A (GZMA) and perforin (PRF1) gene expression, as described in (32). All these signatures are given in the 2nd tab of **Data S2**.

Label Transfer

In order to validate the CAF-S1 clusters identified in the first dataset, another set of data corresponding to 1582 CAF-S1 fibroblasts after quality control and collected from an additive BC sample was analyzed using Seurat pipeline. The Label Transfer algorithm, described in (28) and implemented in Seurat V3.0 R package, was applied using functions *FindTransferAnchors* and *TransferData*. The first dataset of 18 296 CAF-S1 cells was used as reference, while the second dataset of 1582 CAF-S1 cells was used as query. When finding anchors, dimensional reduction was performed by projecting the PCA from the reference onto the query. 30 dimensions were used.

Single-cell data integration from BC, HNSCC and NSCLC

Integration between BC and HNSCC or BC and NSCLC single-cell data was done using method described in (28) and implemented in Seurat V3.0 R package. In brief, the identification of cell pairwise correspondences between single cells across datasets (called “anchors”) allows transforming datasets into a shared space. Dimensionality reduction of both datasets was performed using diagonalized Canonical Correspondence Analysis (CCA) and L2-normalization was applied to the canonical correlation vectors prior to the identification of anchors. Default parameters were used for *FindIntegrationAnchors* and *IntegrateData* function in Seurat V3.0 package.

Flow cytometry analysis of the 5 most abundant CAF-S1 clusters and immune cells

44 BC were cut into small fragments and digested in CO_2-independent medium (Gibco, #18045-054) supplemented with 5% fetal bovine serum (FBS, PAA, #A11-151), 2 mg/ml collagenase I (Sigma-Aldrich, #C0130), 2 mg/ml hyaluronidase (Sigma-Aldrich, #H3506) and 25 mg/ml DNase I (Roche, #11284932001) for 45 min at 37°C with shaking (180 rpm). After tissue digestion, cells were filtered using a cell strainer (40 mm, Fischer Scientific, #223635447) and washed using PBS solution (Gibco, #14190) supplemented with 2 mM EDTA (Gibco, #15575) and 1% human serum (BioWest, #S4190-100). Cells were then separated on 2 groups for analyzing CAF-S1 clusters panel and immune cells panel, respectively.

CAF-S1 clusters panel: Cells were stained with Live Dead NIR (1:1000, BD Bioscience #565388) for 20 min in PBS. Cells were then washed and stained with an antibody cocktail for 45 min containing anti-CD235a-APC-Cy7 (1:20, BioLegend, #349115) anti-EpCAM-BV605 (1:25, Biolegend, #324224), anti-CD31-PECy7 (1:50, BioLegend, #303118), anti-CD45-BUV395 (1:25, BD Biosciences, #BD-563792), anti-CD29-Alexa Fluor 700 (1:50, BioLegend, #303020), anti-FAP (1:100, R&D Systems, #MAB3715) coupled using fluorescent dye Zenon APC Mouse IgG1 labeling kit (Thermo Fisher Scientific, #Z-25051), anti-ANTXR1-AF405 (1:33, Novus Biological, #NB-100-56585), anti-LAMP5-PE (1:10, Miltenyi Biotech, #130-109-156), anti-SDC1-BUV737 (1:25, BD Biosciences, #BD-564393), anti GPC3-AF594 (1:20, RnD, #FAB2119T,100UG), anti-DLK1-AF488 (1:25, RnD, #FAB1144G-100) and anti-CD9-BV711 (1:200, BD Biosciences, #BD-743050). Isotype control antibodies for each CAF cluster marker used were: mouse IgG1 isotype control - BV711 (1:200, BD Bioscience, #563044), mouse IgG1 isotype control - AF405 (1:3, Novus Biological, #IC002V), mouse IgG1 isotype control - BUV737 (1:25, BD Bioscience, #564299), mouse IgG2B isotype control - AF488 (1:12,5, RnD, #IC0041G), mouse IgG2A isotype control - AF594 (1:5, RnD, #IC003T), REA Control-PE (1:10, Miltenyi Biotech, #130-113-462). Cells were then washed and acquired using LSR FORTESSA analyzer (BD biosciences) the same day or fixed in 4% paraformaldehyde (PFA, Electron Microscopy Sciences, #15710) for 20 minutes then washed and kept in PBS+ solution overnight and acquired the next day. At least 5 x 10^5 events were recorded. Compensations were performed using single staining on anti-mouse IgG and negative control beads (BD bioscience #552843) for each antibody and on cells for Live/Dead staining. Data analysis was performed using FlowJo version 10.4.2 (LLC, USA). Cells were first gated based on forward (FSC-A) and side (SSC-A) scatters (measuring cell size and granulosity, respectively) to exclude debris. Dead cells and red blood cells were excluded based on their positive staining for Live/Dead NIR and CD235a respectively. Single cells were next selected based on SSC-H versus SSC-A parameters. Cells were then gated on $EpCAM^-$, $CD45^-$, $CD31^-$ cells, for excluding epithelial cells ($EpCAM^+$), hematopoietic cells ($CD45^+$) and endothelial cells ($CD31^+$). $DAPI^-$, $EPCAM^-$, $CD45^-$, $CD31^-$ cells were separated on 4 subsets (CAF-S1 to CAF-

S4) according to FAP and CD29. CAF-S1 subset was first gated on ANTXR1. ANTXR1^{+} cells were next gated according to SDC1 and LAMP5. ANTXR1^{+} SDC1^{+} LAMP5^{-} were defined as cluster 0/ecm-myCAF and ANTXR1^{+} SDC1^{-} LAMP5^{+} as cluster 3/TGFβ-myCAF. ANTXR1^{+} SDC1^{-} LAMP5^{-} were gated on CD9, and ANTXR1^{+} SDC1^{-} LAMP5^{-} CD9^{+} were defined as cluster 4/ wound-myCAF. ANTXR1$^{-/Low}$ cells were gated on DLK1 and GPC3. Cluster 1/detox-iCAF was defined as ANTXR1^{-} GPC3^{+} DLK1$^{-/+}$ and cluster 2 as ANTXR1^{-} GPC3^{-} DLK1^{+}. ANTXR1^{-} GPC3^{-} DLK1^{-} and ANTXR1^{+} SDC1^{-} LAMP5^{-} CD9^{-} were designated as other clusters. *Immune panel:* Among the 44 BC samples analyzed for CAF-S1 clusters, 37 were characterized at the meantime for immune content. Cell types were analyzed on the live dead negative fraction and defined as hematopoietic cell (CD45^{+}), CD4^{+} / CD8^{+} T lymphocytes; B lymphocytes (CD45^{+} CD14^{-}CD3^{-} CD19^{+}); NK (CD45^{+} CD14^{-} CD3^{-} CD56^{+}), cytotoxic NK (CD56^{+} CD16^{+}) and non-cytotoxic NK (CD56^{+} CD16^{-}); (CD45^{+} CD14^{-} CD3^{+} CD4^{+} / CD8^{+}) and myeloid cells (CD45^{+} CD14^{+}). On each identified population, the percentage of positive cells for the following checkpoints was also evaluated: PD-1, CTLA-4, NKG2A, TIGIT, CD244, CD158K, CD69, CD161. Cells were stained with Live dead (1:1000, Thermo Fisher Scientific, #L34955) for 20 min in PBS. Cells were then washed and stained with an antibody cocktail for 45 min containing anti-CD45-APC-cy7 (1:20, BD Biosciences, #BD-557833); anti-CD14-BV510 (1:50, BD Bioscience, #563079), anti-CD56-BUV395 (1:25, BD Bioscience, #563554), anti-CD16-BV650 (1:25, BD Bioscience, #563692), anti-PD-1-BUV 737 (1:20, BD Bioscience, #565299) anti-CD3-AF700 (1:25, BD Bioscience, #557943), anti-NKG2A-BV786 (1:20, BD Bioscience, #747917), anti-TIGIT-BV605 (1:20, BD Bioscience, #747841), anti-CD158K-PE (1:10, Miltenyi Biotech, #130-095-205) anti-CD244-FITC (1:10, BD Bioscience, #550815), anti-CTLA-4-Pe-cy5 (1:10, BD Bioscience, #555854), anti-CD19-Percp-cy5.5 (1:20, BD Bioscience, #561295), anti-CD4 APC (1:25, Miltenyi Biotec, #130-092-374), anti-CD8-PE-TexasRred (1:100, Life Technologies, #MHCD0817), anti-CD69-BV710 (1:25, BD Bioscience, #563836), anti-CD161-PE-VIO770 (1:100, Miltenyi, #130-113-597). Cells were then washed and acquired using LSR FORTESSA analyzer (BD biosciences) the same day or fixed in 4% paraformaldehyde (PFA, Electron Microscopy Sciences, #15710) for 20 minutes then washed and kept in PBS+ solution

overnight and acquired the next day. At least 5 x 10^5 events were recorded. Compensations were performed using single staining on anti-mouse IgG and negative control beads (BD bioscience, #552843) for each antibody and on cells for Live/Dead staining. Data analysis was performed using FlowJo version 10.4.2 (LLC, USA).

RNA sequencing of CAF-S1 primary cell lines isolated from BC

RNAs were extracted from CAF-S1 fibroblasts with Qiagen miRNeasy kit (Qiagen, #217004) according to the manufacturer's instructions. Among the 7 CAF-S1 primary cell lines studied here, 3 were isolated by sorting and 4 by spreading. These 7 CAF-S1 primary cell lines were generated from 7 different BC patients. RNA integrity and quality were analyzed using the Agilent RNA 6000 Pico kit (Agilent Technologies, #5067-1513). cDNA libraries were prepared using the TruSeq Stranded mRNA kit (Illumina, #20020594) followed by sequencing on NovaSeq (Illumina). Reads were mapped on the human reference genome (hg38; Gencode release 26) and quantified using STAR (version 2.5.3a) with parameters "outFilterMultimapNmax = 20; alignSJoverhangMin = 8; alignSJDBoverhangMin = 1; outFilterMismatchNmax = 999; outFilterMismatchNoverLmax = 0.04; alignIntronMin = 20; alignIntronMax = 1000000; alignMatesGapMax = 1000000; outMultimapperOrder = Random". Only genes with one read in at least 5% of all samples were kept for further analyses. Normalization were conducted with DESeq2 R package and raw read matrix was log2 transformed. For identifying the identity of CAF-S1 primary cell lines, a score was computed by the mean of expression of the genes that compose the iCAF/myCAF signatures (as defined in (7) and for each CAF-S1 cluster signature (as defined in this paper, and shown in **Data S2**). P values are from DESeq2 analysis.

Functional assays

Isolation of $CD4^+$ $CD25^+$ T lymphocytes: $CD4^+$ $CD25^+$ T lymphocytes were isolated from peripheral blood of healthy donors obtained from the ''Etablissement Français du Sang'', Paris, Saint-Antoine Crozatier blood bank through a convention with the Institut Curie (Paris, France).

Briefly, peripheral blood mononuclear cells (PBMCs) were isolated using Lymphoprep (Stemcell, #07861), as previously described in (8). $CD4^+$ CD25+ were purified from 5 x 10^8 PBMC by using magnetic cell separation (MACS) with the human $CD4^+$ $CD25^+$ Tregs isolation kit (Miltenyi Biotec, #130-091-301), according to manufacturer's instructions. The purity of $CD4^+$ $CD25^+$ T lymphocytes was determined by flow cytometry, as described in (8).

Isolation of CAF-S1 clusters in culture: To isolate the different CAF-S1 clusters, we first started by sorting the cells according to their specific markers but we failed to keep them alive with their different identities. We then tested two distinct methods of isolation by spreading and sorting. For the "spreading" method, tumors were cut into small pieces and incubated in plastic dishes (Falcon, #353003) in DMEM (HyClone, #SH30243.01) supplemented with 10% FBS (Biosera, #FB-1003/500), streptomycin (100 µg/ml) and penicillin (100 U/ml) (Gibco #15140-122) in a humidified in 1.5% O_2 and 5% CO_2 incubator, to let fibroblasts spread and expand during at least 2-3 weeks at 37ºC. For isolating fibroblasts by the "sorting" method, tumors were digested using enzymatic cocktails described in (# *Isolation of CAF-S1 from BC)* and sorted by BDFACS ARIA III^{TM} using the gating strategy detailed in *(#CAF-S1 RNA sequencing at single cell*) in 48-well plastic dishes (TPP plates, #192048) pre-coated with FBS for 2h. CAF-S1 sorted cells were next expanded during 3-4 weeks at 37ºC in plastic dishes (TPP plates, #192048) in pericyte medium (ScienCell, #1201) supplemented with 2% FBS (ScienCell, #0010) in a humidified in 1.5% O_2 and 5% CO_2 incubator. For comparing cellular identity of sorted and spread CAF-S1 fibroblasts in the exact same conditions used in functional assays, both types of fibroblasts (spread and sorted) were transferred into plastic dishes (Falcon, #353047) in DMEM medium (HyClone, #SH30243.01) in 20% O_2, as these culture conditions are compatible with co-culture with CD4+ CD25+ T lymphocytes which are applied for *in vitro* functional assays. Using these protocols, 7 different CAF-S1 cell lines from 7 different patients have been isolated, 3 by sorting and 4 by spreading. To avoid any *in vitro* activation, these CAF-S1 primary cell lines isolated by sorting and spreading were used no later than passage 5. Moreover, in each experiment, properties of spread and sorted cells were compared at the same passages.

Treg - CAF-S1 clusters functional assays: 5x10^4 CAF-S1 cells (spread and sorted) were plated on 24-well plates (Falcon, #353047) in DMEM (HyClone, #SH30243.01) with 10% FBS (Biosera, # FB-1003/500) at 1.5% O_2 overnight for complete adherence. The medium was then removed and 5x10^5 CD4$^+$ CD25$^+$ T lymphocytes were added in 500µl of DMEM 1% FBS (ratio 1-10) and incubated overnight (for RNA analysis) or for 24h (for FACS) at 37°C, 20% O_2. For FACS analysis, non-adherent cells (CD4$^+$ CD25$^+$) were then harvested, washed and stained for 30 min at RT using the following markers: Live Dead (1:1000, BD Bioscience, #562247), anti-CD45-BUV395 (1:50, BD Biosciences, #BD-563792), anti-CD4-APC (1:50, Miltenyi Biotec, #130-092-374), anti-CD25 PE-cy7 (1:33, BD Bioscience, #557741), anti-FOXP3-FITC (1:33, ebioscience, #53-4776-42), anti-CTLA-4-Pe-cy5 (1:20, BD Bioscience,# 555854), anti-PD-1-BUV737 (BD Bioscience,# 565299), anti-TIGIT-BV605 (1:50, BD Bioscience, # 747841), anti-LAG3-BV510 (1:50, BD Bioscience, #744985), anti-TIM3-BV711 (1:50, BD Bioscience, #565566). Adherent cells were trypsinized, washed and stained for CAF-S1 clusters markers (ANTXR1, CD9, SDC1, LAMP5, GPC3, DLK1) in addition to Live Dead NIR to remove dead cells and CD45 to remove remaining Tregs. Cells (Treg Panel and CAF-S1 panel) were acquired using ZE5 cell analyzer (Bio-Rad) and analyzed by Flowjo v10.4.2. For RNA analysis, non-adherent cells (CD4$^+$ CD25$^+$) were harvested by pipetting, and spin down. RNA was then extracted using Single Cell RNA Purification Kit (Norgen Biotek corp., #51800) according to the manufacturer's recommendations. RNA integrity and quality were analyzed using the Agilent RNA 6000 Pico kit (Agilent Technologies, #5067-1513). cDNA libraries were prepared using the TruSeq RNA Exome kit (Illumina, #20020189) followed by sequencing on NovaSeq (Illumina). Reads were mapped on the human reference genome (hg38; Gencode release 29) and quantified using STAR (version 2.6.1a) with parameters "outFilterMultimapNmax = 20; alignSJoverhangMin = 8; alignSJDBoverhangMin = 1; outFilterMismatchNmax = 999; outFilterMismatchNoverLmax = 0.04; alignIntronMin = 20; alignIntronMax = 1000000; alignMatesGapMax = 1000000; outMultimapperOrder = Random". Only genes with one read in at least 5% of all samples were kept for further analyses. Normalization was conducted with DESeq2 R package.

Treg - CAF-S1 cluster intracellular staining: $5x10^4$ CAF-S1 cells (spread) were plated on 24-well plates (Falcon, #353047) in DMEM (HyClone, #SH30243.01) with 10% FBS (Biosera, # FB-1003/500) at 1.5% O_2 overnight for complete adherence. The medium was then removed and $5x10^5$ $CD4^+$ $CD25^+$ T lymphocytes were added in 500µl of DMEM 1% FBS (ratio 1-10) and incubated overnight at 37°C, 20% O_2. Non-adherent cells ($CD4^+$ $CD25^+$) were then harvested, washed and stained for 30 min at RT with Live Dead (1:1000, BD Bioscience, #562247),after washing, the cells were divided in 2 groups (one fixed and permeabilized and the second kept without fixation / permeabilization except for FOXP3 staining) and stained using the following markers: anti-CD45-BUV395 (1:50, BD Biosciences, #BD-563792), anti-CD4-APC (1:50, Miltenyi Biotec, #130-092-374), anti-CD25 PE-cy7 (1:33, BD Bioscience, #557741), anti-CTLA-4-Pe-cy5 (1:20, BD Bioscience,# 555854), anti-PD-1-BUV737 (BD Bioscience,# 565299), anti-TIGIT-BV605 (1:50, BD Bioscience, # 747841), anti-LAG3-BV510 (1:50, BD Bioscience, #744985), anti-TIM3-BV711 (1:50, BD Bioscience, #565566) anti-FOXP3-FITC (1:33, ebioscience, #53-4776-42)

Comparison of fibroblasts from normal healthy tissue with CAF-S1 from BC

Primary fibroblasts were collected by using the spreading method (see above) from juxta-tumors, i.e. tissues defined as heathy by referent Pathologists. Juxta-tumors were cut into small pieces, put in plastic dishes (Falcon, #353003) and cultured in DMEM (HyClone, #SH30243.01) supplemented with 10% FBS (Biosera, #FB-1003/500), streptomycin (100 µg/ml) and penicillin (100 U/ml) (Gibco #15140122) for 2-3 weeks at 37ºC. Spread fibroblasts were next analyzed at early and late passages (passages 2 and 5, respectively) for verifying expression of CAF-S1 markers. Primary cells were trypsinized, resuspended in PBS and stained with LIVE/DEAD™ Fixable Aqua Dead Cell Stain dye (ThermoFisher Scientific, #L34957) diluted in PBS for 20 min at RT and fixed in PFA 4% for 20 min at RT. After a rapid wash in PBS+, the cells were stained with an anti-FAP antibody (1:100, R&D Systems, #MAB3715) or isotype control (1:100, R&D Systems, #MAB002) in PBS+ for 40 min at RT. Both antibody and isotype control were coupled using fluorescent dye Zenon APC Mouse IgG1

labeling kit (Thermo Fisher Scientific, #Z-25051). Cells were acquired using LSR FORTESSA analyzer (BD biosciences). 50 000 events per sample were recorded.

RNA sequencing from NSCLC samples

Formalin Fixed Paraffin Embedded (FFPE) biopsies (N = 120) from NSCLC naïve from any treatment were processed for RNA extraction using high FFPET RNA Isolation Kit (Roche, #06650775001) following the manufacturer's instructions. RNA integrity and quality were analyzed using the Agilent RNA 6000 Pico kit (Agilent Technologies, #5067-1513). Samples with a DV200 higher than 40% were chosen for RNA sequencing (N = 70). cDNA library was prepared using the Nextera XT Sample Preparation kit (Illumina, #FC-131-10) followed by sequencing on NovaSeq (Illumina). Reads were mapped on the human reference genome (release hg19/GRCh37) and quantified using STAR (version 2.5.3a) with parameters "outFilterMultimapNmax = 20; alignSJoverhangMin = 8; alignSJDBoverhangMin = 1; outFilterMismatchNmax = 999; outFilterMismatchNoverLmax = 0.04; alignIntronMin = 20; alignIntronMax = 1000000; alignMatesGapMax = 1000000; outMultimapperOrder = Random". Only genes with one read in at least 5% of all samples were kept for further analyses. Normalization, unsupervised analysis (PCA) and differential analysis between responders and non-responders patients were conducted with DESeq2 R package.

Statistical analysis

All statistical analyses and graphical representation of data were performed in the R environment (https://cran.r-project.org, Versions 3.5.3) or using GraphPad Prism software (version 8.1.1). Statistical tests used are in agreement with data distribution: Normality was first checked using the Shapiro–Wilk test and parametric or non-parametric two-tailed tests were applied according to normality, as indicated in each Figure legend. scRNA-seq data presented in **Figs. 1, 2, 3, Fig. S1** and **Fig. S2** were analyzed using *Seurat* R package (version 3.0). Correlation matrix shown in **Figs. 2** and **4** were computed using *cor* function from *stats* R package with method = "pearson" and use = "pairwise.complete.obs". *Corrplot* R function was

used for the clustering and the visualization of the correlation matrix with following parameters: *order* = “hclust” and *hclust.method* = “ward.D2”. Quantifications from FACS analysis shown in **Fig. 5** are shown using mean ± s.e.m. Differential analysis between $CD4^+$ $CD25^+$ T cells cultured alone or in presence of ecm-myCAF in **Fig. S4D** and **Fig. S4E** were conducted using DESeq2 R package. Gene Set Enrichment Analysis (GSEA) software version 3.0 (Broad Institute) was used in **Fig. 6**. For melanoma RNA-seq data, the following parameters were applied: Enrichment statistic = ‘weighted’, Metric for ranking genes = ‘Signal2Noise’. For NSCLC RNA-seq data, GSEAPreranked was used with log2 fold change from DESeq2 differential analysis as metric for ranking genes and ‘classic’ mode for enrichment score.

REFERENCES

1. Pietras K, Ostman A. Hallmarks of cancer: interactions with the tumor stroma. Exp Cell Res **2010**;316(8):1324-31 doi 10.1016/j.yexcr.2010.02.045.
2. Toullec A, Gerald D, Despouy G, Bourachot B, Cardon M, Lefort S*, et al.* Oxidative stress promotes myofibroblast differentiation and tumour spreading. EMBO Mol Med **2010**;2(6):211-30 doi 10.1002/emmm.201000073.
3. Hanahan D, Coussens LM. Accessories to the crime: functions of cells recruited to the tumor microenvironment. Cancer Cell **2012**;21(3):309-22 doi 10.1016/j.ccr.2012.02.022.
4. Costa A, Scholer-Dahirel A, Mechta-Grigoriou F. The role of reactive oxygen species and metabolism on cancer cells and their microenvironment. Semin Cancer Biol **2014**;25:23-32 doi 10.1016/j.semcancer.2013.12.007.
5. Kalluri R. The biology and function of fibroblasts in cancer. Nat Rev Cancer **2016**;16(9):582-98 doi 10.1038/nrc.2016.73.
6. Sahai E, Astsaturov I, Cukierman E, DeNardo DG, Egeblad M, Evans RM*, et al.* A framework for advancing our understanding of cancer-associated fibroblasts. Nat Rev Cancer **2020**;20(3):174-86 doi 10.1038/s41568-019-0238-1.
7. Ohlund D, Handly-Santana A, Biffi G, Elyada E, Almeida AS, Ponz-Sarvise M*, et al.* Distinct populations of inflammatory fibroblasts and myofibroblasts in pancreatic cancer. J Exp Med **2017**;214(3):579-96 doi 10.1084/jem.20162024.
8. Costa A, Kieffer Y, Scholer-Dahirel A, Pelon F, Bourachot B, Cardon M*, et al.* Fibroblast Heterogeneity and Immunosuppressive Environment in Human Breast Cancer. Cancer Cell **2018**;33(3):463-79 e10 doi 10.1016/j.ccell.2018.01.011.
9. Cremasco V, Astarita JL, Grauel AL, Keerthivasan S, MacIsaac K, Woodruff MC*, et al.* FAP Delineates Heterogeneous and Functionally Divergent Stromal Cells in Immune-Excluded Breast Tumors. Cancer Immunol Res **2018**;6(12):1472-85 doi 10.1158/2326-6066.CIR-18-0098.
10. Givel AM, Kieffer Y, Scholer-Dahirel A, Sirven P, Cardon M, Pelon F*, et al.* miR200-regulated CXCL12beta promotes fibroblast heterogeneity and immunosuppression in ovarian cancers. Nat Commun **2018**;9(1):1056 doi 10.1038/s41467-018-03348-z.
11. Mariathasan S, Turley SJ, Nickles D, Castiglioni A, Yuen K, Wang Y*, et al.* TGFbeta attenuates tumour response to PD-L1 blockade by contributing to exclusion of T cells. Nature **2018**;554(7693):544-8 doi 10.1038/nature25501.
12. Raz Y, Cohen N, Shani O, Bell RE, Novitskiy SV, Abramovitz L*, et al.* Bone marrow-derived fibroblasts are a functionally distinct stromal cell population in breast cancer. J Exp Med **2018**;215(12):3075-93 doi 10.1084/jem.20180818.
13. Su S, Chen J, Yao H, Liu J, Yu S, Lao L*, et al.* CD10(+)GPR77(+) Cancer-Associated Fibroblasts Promote Cancer Formation and Chemoresistance by Sustaining Cancer Stemness. Cell **2018**;172(4):841-56 e16 doi 10.1016/j.cell.2018.01.009.
14. Neuzillet C, Tijeras-Raballand A, Ragulan C, Cros J, Patil Y, Martinet M*, et al.* Inter- and intra-tumoural heterogeneity in cancer-associated fibroblasts of human pancreatic ductal adenocarcinoma. J Pathol **2019**;248(1):51-65 doi 10.1002/path.5224.
15. Strell C, Paulsson J, Jin SB, Tobin NP, Mezheyeuski A, Roswall P*, et al.* Impact of Epithelial-Stromal Interactions on Peritumoral Fibroblasts in Ductal Carcinoma in Situ. J Natl Cancer Inst **2019**;111(9):983-95 doi 10.1093/jnci/djy234.
16. Elyada E, Bolisetty M, Laise P, Flynn WF, Courtois ET, Burkhart RA*, et al.* Cross-Species Single-Cell Analysis of Pancreatic Ductal Adenocarcinoma Reveals Antigen-Presenting Cancer-Associated Fibroblasts. Cancer Discov **2019**;9(8):1102-23 doi 10.1158/2159-8290.CD-19-0094.
17. Pelon F, Bourachot B, Kieffer Y, Magagna I, Mermet-Meillon F, Bonnet I*, et al.* Cancer-associated fibroblast heterogeneity in axillary lymph nodes drives metastases in breast cancer through complementary mechanisms. Nat Commun **2020**;11(1):404.

18. Denton AE, Roberts EW, Linterman MA, Fearon DT. Fibroblastic reticular cells of the lymph node are required for retention of resting but not activated CD8+ T cells. Proc Natl Acad Sci U S A **2014**;111(33):12139-44 doi 10.1073/pnas.1412910111.
19. Takahashi H, Sakakura K, Kawabata-Iwakawa R, Rokudai S, Toyoda M, Nishiyama M*, et al.* Immunosuppressive activity of cancer-associated fibroblasts in head and neck squamous cell carcinoma. Cancer Immunol Immunother **2015**;64(11):1407-17 doi 10.1007/s00262-015-1742-0.
20. Ruhland MK, Loza AJ, Capietto AH, Luo X, Knolhoff BL, Flanagan KC*, et al.* Stromal senescence establishes an immunosuppressive microenvironment that drives tumorigenesis. Nat Commun **2016**;7:11762 doi 10.1038/ncomms11762.
21. Yang X, Lin Y, Shi Y, Li B, Liu W, Yin W*, et al.* FAP Promotes Immunosuppression by Cancer-Associated Fibroblasts in the Tumor Microenvironment via STAT3-CCL2 Signaling. Cancer Res **2016**;76(14):4124-35 doi 10.1158/0008-5472.CAN-15-2973.
22. Zhang Y, Ertl HC. Depletion of FAP+ cells reduces immunosuppressive cells and improves metabolism and functions CD8+T cells within tumors. Oncotarget **2016**;7(17):23282-99 doi 10.18632/oncotarget.7818.
23. Cohen N, Shani O, Raz Y, Sharon Y, Hoffman D, Abramovitz L*, et al.* Fibroblasts drive an immunosuppressive and growth-promoting microenvironment in breast cancer via secretion of Chitinase 3-like 1. Oncogene **2017**;36(31):4457-68 doi 10.1038/onc.2017.65.
24. Bartoschek M, Oskolkov N, Bocci M, Lovrot J, Larsson C, Sommarin M*, et al.* Spatially and functionally distinct subclasses of breast cancer-associated fibroblasts revealed by single cell RNA sequencing. Nat Commun **2018**;9(1):5150 doi 10.1038/s41467-018-07582-3.
25. Feig C, Jones JO, Kraman M, Wells RJ, Deonarine A, Chan DS*, et al.* Targeting CXCL12 from FAP-expressing carcinoma-associated fibroblasts synergizes with anti-PD-L1 immunotherapy in pancreatic cancer. Proc Natl Acad Sci U S A **2013**;110(50):20212-7 doi 10.1073/pnas.1320318110.
26. Biffi G, Oni TE, Spielman B, Hao Y, Elyada E, Park Y*, et al.* IL1-Induced JAK/STAT Signaling Is Antagonized by TGFbeta to Shape CAF Heterogeneity in Pancreatic Ductal Adenocarcinoma. Cancer Discov **2019**;9(2):282-301 doi 10.1158/2159-8290.CD-18-0710.
27. Tirosh I, Izar B, Prakadan SM, Wadsworth MH, Treacy D, Trombetta JJ*, et al.* Dissecting the multicellular ecosystem of metastatic melanoma by single-cell RNA-seq. Science **2016**;352(6282):189-96 doi 10.1126/science.aad0501.
28. Stuart T, Butler A, Hoffman P, Hafemeister C, Papalexi E, Mauck WM, 3rd*, et al.* Comprehensive Integration of Single-Cell Data. Cell **2019**;177(7):1888-902 e21 doi 10.1016/j.cell.2019.05.031.
29. Dominguez CX, Muller S, Keerthivasan S, Koeppen H, Hung J, Gierke S*, et al.* Single-Cell RNA Sequencing Reveals Stromal Evolution into LRRC15(+) Myofibroblasts as a Determinant of Patient Response to Cancer Immunotherapy. Cancer Discov **2020**;10(2):232-53 doi 10.1158/2159-8290.CD-19-0644.
30. Puram SV, Tirosh I, Parikh AS, Patel AP, Yizhak K, Gillespie S*, et al.* Single-Cell Transcriptomic Analysis of Primary and Metastatic Tumor Ecosystems in Head and Neck Cancer. Cell **2017**;171(7):1611-24 e24 doi 10.1016/j.cell.2017.10.044.
31. Lambrechts D, Wauters E, Boeckx B, Aibar S, Nittner D, Burton O*, et al.* Phenotype molding of stromal cells in the lung tumor microenvironment. Nat Med **2018**;24(8):1277-89 doi 10.1038/s41591-018-0096-5.
32. Rooney MS, Shukla SA, Wu CJ, Getz G, Hacohen N. Molecular and genetic properties of tumors associated with local immune cytolytic activity. Cell **2015**;160(1-2):48-61 doi 10.1016/j.cell.2014.12.033.
33. Hugo W, Zaretsky JM, Sun L, Song C, Moreno BH, Hu-Lieskovan S*, et al.* Genomic and Transcriptomic Features of Response to Anti-PD-1 Therapy in Metastatic Melanoma. Cell **2016**;165(1):35-44 doi 10.1016/j.cell.2016.02.065.

34. Patel AP, Tirosh I, Trombetta JJ, Shalek AK, Gillespie SM, Wakimoto H*, et al.* Single-cell RNA-seq highlights intratumoral heterogeneity in primary glioblastoma. Science **2014**;344(6190):1396-401 doi 10.1126/science.1254257.
35. Kim KT, Lee HW, Lee HO, Song HJ, Jeong da E, Shin S*, et al.* Application of single-cell RNA sequencing in optimizing a combinatorial therapeutic strategy in metastatic renal cell carcinoma. Genome Biol **2016**;17:80 doi 10.1186/s13059-016-0945-9.
36. Tirosh I, Venteicher AS, Hebert C, Escalante LE, Patel AP, Yizhak K*, et al.* Single-cell RNA-seq supports a developmental hierarchy in human oligodendroglioma. Nature **2016**;539(7628):309-13 doi 10.1038/nature20123.
37. Chung W, Eum HH, Lee HO, Lee KM, Lee HB, Kim KT*, et al.* Single-cell RNA-seq enables comprehensive tumour and immune cell profiling in primary breast cancer. Nat Commun **2017**;8:15081 doi 10.1038/ncomms15081.
38. Li H, Courtois ET, Sengupta D, Tan Y, Chen KH, Goh JJL*, et al.* Reference component analysis of single-cell transcriptomes elucidates cellular heterogeneity in human colorectal tumors. Nat Genet **2017**;49(5):708-18 doi 10.1038/ng.3818.
39. Venteicher AS, Tirosh I, Hebert C, Yizhak K, Neftel C, Filbin MG*, et al.* Decoupling genetics, lineages, and microenvironment in IDH-mutant gliomas by single-cell RNA-seq. Science **2017**;355(6332) doi 10.1126/science.aai8478.
40. Karaayvaz M, Cristea S, Gillespie SM, Patel AP, Mylvaganam R, Luo CC*, et al.* Unravelling subclonal heterogeneity and aggressive disease states in TNBC through single-cell RNA-seq. Nat Commun **2018**;9(1):3588 doi 10.1038/s41467-018-06052-0.
41. Kim C, Gao R, Sei E, Brandt R, Hartman J, Hatschek T*, et al.* Chemoresistance Evolution in Triple-Negative Breast Cancer Delineated by Single-Cell Sequencing. Cell **2018**;173(4):879-93 e13 doi 10.1016/j.cell.2018.03.041.
42. Wang X, Allen WE, Wright MA, Sylwestrak EL, Samusik N, Vesuna S*, et al.* Three-dimensional intact-tissue sequencing of single-cell transcriptional states. Science **2018**;361(6400) doi 10.1126/science.aat5691.
43. Bernard V, Semaan A, Huang J, San Lucas FA, Mulu FC, Stephens BM*, et al.* Single-Cell Transcriptomics of Pancreatic Cancer Precursors Demonstrates Epithelial and Microenvironmental Heterogeneity as an Early Event in Neoplastic Progression. Clin Cancer Res **2019**;25(7):2194-205 doi 10.1158/1078-0432.CCR-18-1955.
44. Wagner J, Rapsomaniki MA, Chevrier S, Anzeneder T, Langwieder C, Dykgers A*, et al.* A Single-Cell Atlas of the Tumor and Immune Ecosystem of Human Breast Cancer. Cell **2019**;177(5):1330-45 e18 doi 10.1016/j.cell.2019.03.005.
45. Lavin Y, Kobayashi S, Leader A, Amir ED, Elefant N, Bigenwald C*, et al.* Innate Immune Landscape in Early Lung Adenocarcinoma by Paired Single-Cell Analyses. Cell **2017**;169(4):750-65 e17 doi 10.1016/j.cell.2017.04.014.
46. Lee HO, Park WY. Single-cell RNA-Seq unveils tumor microenvironment. BMB Rep **2017**;50(6):283-4.
47. Zheng C, Zheng L, Yoo JK, Guo H, Zhang Y, Guo X*, et al.* Landscape of Infiltrating T Cells in Liver Cancer Revealed by Single-Cell Sequencing. Cell **2017**;169(7):1342-56 e16 doi 10.1016/j.cell.2017.05.035.
48. Schelker M, Feau S, Du J, Ranu N, Klipp E, MacBeath G*, et al.* Estimation of immune cell content in tumour tissue using single-cell RNA-seq data. Nat Commun **2017**;8(1):2032 doi 10.1038/s41467-017-02289-3.
49. Azizi E, Carr AJ, Plitas G, Cornish AE, Konopacki C, Prabhakaran S*, et al.* Single-Cell Map of Diverse Immune Phenotypes in the Breast Tumor Microenvironment. Cell **2018**;174(5):1293-308 doi 10.1016/j.cell.2018.05.060.
50. Kumar MP, Du J, Lagoudas G, Jiao Y, Sawyer A, Drummond DC*, et al.* Analysis of Single-Cell RNA-Seq Identifies Cell-Cell Communication Associated with Tumor Characteristics. Cell Rep **2018**;25(6):1458-68 e4 doi 10.1016/j.celrep.2018.10.047.
51. Zhang L, Zhang Z. Recharacterizing Tumor-Infiltrating Lymphocytes by Single-Cell RNA Sequencing. Cancer Immunol Res **2019**;7(7):1040-6 doi 10.1158/2326-6066.CIR-18-0658.

52. Tumeh PC, Harview CL, Yearley JH, Shintaku IP, Taylor EJ, Robert L*, et al.* PD-1 blockade induces responses by inhibiting adaptive immune resistance. Nature **2014**;515(7528):568-71 doi 10.1038/nature13954.
53. Sharma P, Hu-Lieskovan S, Wargo JA, Ribas A. Primary, Adaptive, and Acquired Resistance to Cancer Immunotherapy. Cell **2017**;168(4):707-23 doi 10.1016/j.cell.2017.01.017.
54. Kim TK, Herbst RS, Chen L. Defining and Understanding Adaptive Resistance in Cancer Immunotherapy. Trends Immunol **2018**;39(8):624-31 doi 10.1016/j.it.2018.05.001.
55. Shalapour S, Karin M. Pas de Deux: Control of Anti-tumor Immunity by Cancer-Associated Inflammation. Immunity **2019**;51(1):15-26 doi 10.1016/j.immuni.2019.06.021.
56. Tauriello DVF, Palomo-Ponce S, Stork D, Berenguer-Llergo A, Badia-Ramentol J, Iglesias M*, et al.* TGFbeta drives immune evasion in genetically reconstituted colon cancer metastasis. Nature **2018**;554(7693):538-43 doi 10.1038/nature25492.
57. Gonzalez-Junca A, Driscoll KE, Pellicciotta I, Du S, Lo CH, Roy R*, et al.* Autocrine TGFbeta Is a Survival Factor for Monocytes and Drives Immunosuppressive Lineage Commitment. Cancer Immunol Res **2019**;7(2):306-20 doi 10.1158/2326-6066.CIR-18-0310.
58. Powles T, Kockx M, Rodriguez-Vida A, Duran I, Crabb SJ, Van Der Heijden MS*, et al.* Clinical efficacy and biomarker analysis of neoadjuvant atezolizumab in operable urothelial carcinoma in the ABACUS trial. Nat Med **2019**;25(11):1706-14 doi 10.1038/s41591-019-0628-7.
59. Wang L, Saci A, Szabo PM, Chasalow SD, Castillo-Martin M, Domingo-Domenech J*, et al.* EMT- and stroma-related gene expression and resistance to PD-1 blockade in urothelial cancer. Nat Commun **2018**;9(1):3503 doi 10.1038/s41467-018-05992-x.
60. Zhao F, Evans K, Xiao C, DeVito N, Theivanthiran B, Holtzhausen A*, et al.* Stromal Fibroblasts Mediate Anti-PD-1 Resistance via MMP-9 and Dictate TGFbeta Inhibitor Sequencing in Melanoma. Cancer Immunol Res **2018**;6(12):1459-71 doi 10.1158/2326-6066.CIR-18-0086.
61. Salmon H, Franciszkiewicz K, Damotte D, Dieu-Nosjean MC, Validire P, Trautmann A*, et al.* Matrix architecture defines the preferential localization and migration of T cells into the stroma of human lung tumors. J Clin Invest **2012**;122(3):899-910 doi 10.1172/JCI45817.
62. Hellmann MD, Paz-Ares L, Bernabe Caro R, Zurawski B, Kim SW, Carcereny Costa E*, et al.* Nivolumab plus Ipilimumab in Advanced Non-Small-Cell Lung Cancer. N Engl J Med **2019**;381(21):2020-31 doi 10.1056/NEJMoa1910231.
63. Butler A, Hoffman P, Smibert P, Papalexi E, Satija R. Integrating single-cell transcriptomic data across different conditions, technologies, and species. Nat Biotechnol **2018**;36(5):411-20 doi 10.1038/nbt.4096.

FIGURE LEGENDS

Figure 1: Identification of distinct cellular clusters in CAF-S1 fibroblasts

(**A**) Uniform Manifold Approximation and Projection (UMAP) of 18 296 CAF-S1 fibroblasts across 7 BC patients allowing the visualization of 8 CAF-S1 clusters (0 to 7). Colors show the different CAF-S1 clusters defined by graph-based clustering method applied on the space defined by the 30 first principal components. (**B, C**) Same UMAP plots as in (**A**) showing patients (P1 to P7) (**B**) and breast cancer subtypes (Lum for luminal in red; TN for triple-negative in blue) (**C**) from which each CAF-S1 fibroblast is derived. (**D**) UMAP (upper panel) and violin plot (lower panel) showing expression of 2 representative genes for each CAF-S1 cluster. (**E, F**) UMAP (upper panel) showing mean expression of the top-25 genes of iCAF (**E**) and myCAF (**F**) signatures, defined in (7). UMAP and violin plot (lower panels) showing expression of 2 representative genes for iCAF and myCAF subgroups, as indicated. (**G**) Same as in (**D**) for CD74, a specific marker of apCAF, as shown in (16).

Figure 2: Validation of the 5 most abundant CAF-S1 clusters in distinct cancer types

(**A**) Percentage (%) of the different clusters among CAF-S1 fibroblasts based on scRNA-seq data, each CAF-S1 cell being attributed as shown in Fig. 1A. (**B**) UMAP plots showing RNA levels of surface markers that are specific of each CAF-S1 cluster, also shown in colors as in Fig. 1A. (**C**) FACS plots from a representative BC patient showing the gating strategy used for validating the 5 most abundant CAF-S1 clusters shown in (**B**) by combining protein surface markers. Gating strategy is as followed: Among FAP^{High} $CD29^{Med}$ CAF-S1, $ANTXR1^{+}$ cells (myCAF) were next gated based on SDC1, LAMP5 and CD9; $ANTXR1^{-}$ cells (iCAF) on GPC3 and DLK1. Clusters were defined as followed: cluster 0/ecm-myCAF: $ANTXR1^{+}$ $SDC1^{+}$ $LAMP5^{-}$; cluster 3/TGFβ-myCAF: $ANTXR1^{+}$ $SDC1^{+/-}$ $LAMP5^{+}$; cluster 4/wound-myCAF: $ANTXR1^{+}$ $SDC1^{-}$ $LAMP5^{-}$ $CD9^{+}$; cluster 1/detox-iCAF: $ANTXR1^{-}$ $GPC3^{+}$ $DLK1^{+/-}$; cluster 2/IL-iCAF: $ANTXR1^{-}$ $GPC3^{-}$ $DLK1^{+}$. CAF-S1 cells negative for all markers are next called “others”. A representative patient is shown (N = 44 BC patients). (**D**) Percentage (%) of the different clusters among CAF-

S1 fibroblasts based on FACS data. Each bar represents one patient (N = 44). (**E**) Left, Correlation matrix between the content in the 5 most abundant CAF-S1 clusters among total CAF (DAPI^{-} EPCAM^{-} CD45^{-} CD31^{-} CD235a^{-}) and among CAF-S1 fibroblasts (FAP^{High} CD29^{Med}). Data are from FACS (N = 44). P values from Pearson correlation test. The squares show significant positive (red) and negative (blue) correlations. Square sizes are proportional to P value significance and color intensities to the correlation coefficients, standardized from -1 to +1 for heatmap representation, as indicated. Right and bottom: Detailed correlation curves between 2 variables, as indicated. Each dot represents one tumor (N = 44). P values from Pearson correlation test.

Figure 3: Detection of the CAF-S1 cellular clusters in lung and head and neck cancers

(**A**) UMAP plots combining 18 296 CAF-S1 fibroblasts from BC (in red, upper left panel) and FAP^{+} fibroblasts from HNSCC (data from (30), n = 603 FAP^{+} cells, in blue, upper left panel). A score, calculated as the average z-score of genes that compose specific signature of each CAF-S1 cluster, is applied (see **Data S2** for list of genes). (**B**) Same as in (**A**) from NSCLC (data from (31), n = 959 FAP^{+} cells, in blue, upper left panel).

Figure 4: Correlation between CAF-S1 clusters and immune cells in breast cancers

(**A**) **Left,** Correlation matrix between the content in the 5 most abundant CAF-S1 clusters and immune cell sub-populations, all having been quantified by FACS for each patient (N = 37). Data are from FACS (N = 37). P values from Pearson correlation test. The squares show significant positive (red) and negative (blue) correlations. Square sizes are proportional to P value significance and color intensities to the correlation coefficients, standardized from -1 to +1 for heatmap representation, as indicated. Right and bottom: Detailed correlation curves between 2 variables, as indicated. Each dot represents one tumor (N = 37). P values from Pearson correlation test. (**B**) Correlation curves between CAF-S1 cluster signatures and FOXP3 in TCGA cohort. Each dot represents one tumor (N = 1221). P values from Pearson

correlation test. (**C**) Same as in (**B**) between CAF-S1 cluster signatures and cytolytic index, as defined in (32).

Figure 5: Reciprocal effects of CAF-S1 clusters and Tregs

(A) Bar plots showing mean RNA levels of iCAF-, myCAF- and CAF-S1 cluster-signatures in CAF-S1 primary fibroblasts (N = 7 cell lines) isolated from BC either by sorting (N = 3) or spreading (N = 4), as indicated. Identity of CAF-S1 primary cell lines was defined by the mean of expression of iCAF/myCAF gene signatures (defined in (7) and of CAF-S1 cluster signatures (**Data S2**). P values from Student t-test. **(B-G)** Impact of iCAF and myCAF clusters on $FOXP3^+$ $CD4^+$ $CD25^+$ T cells. (**B**) Representative histograms of FOXP3 specific mean fluorescent intensity (speMFI) (Left) either alone (green) or in presence of iCAF (orange) or ecm-myCAF (red). After 24 hours (h) of co-culture with a 10:1 ratio (T:CAF-S1), percentage of $FOXP3^+$ cells (middle) and FOXP3 protein level in $CD4^+$ $CD25^+$ T cells (right) were assessed. P values from Welch's t test (N = 7 CAF-S1 primary cell lines per condition; n = 3 independent experiments). (**C-G**) Same as in (**B**) for the following immune checkpoints, PD-1 **(C)**, CTLA-4 **(D)**, TIGIT **(E),** TIM3 **(F)** and LAG3 **(G)** in $FOXP3^+$ $CD4^+$ $CD25^+$ Tregs. P values from Welch's t-test. (N = 7 CAF-S1 cell lines per condition; n = 3 independent experiments). (**H**) Impact of $CD4^+$ $CD25^+$ T lymphocytes on CAF-S1 cluster identity. Dot plots showing protein levels of CAF-S1 clusters markers at the surface of CAF-S1 primary cell lines. For each marker, surface protein level is expressed as specific MFI, calculated as followed: Specific MFI = MFI from the specific antibody – MFI from the isotype control, in absence (-) or presence (+) of $CD4^+$ $CD25^+$ T cells (N = 7 CAF-S1 cell lines per condition; n = 3 independent experiments). P values from Mann-Whitney test.

Figure 6: Impact of CAF-S1 clusters on resistance to immunotherapies

(**A**) Up, Gene Set Enrichment Analysis (GSEA) applied on RNA-Seq data from 28 melanoma tumors before anti-PD-1 treatment showing significant enrichment of CAF-S1 gene signature (top 100 genes) in non-responding (N = 13) patients, compared to responding (N = 15)

patients. Cohort from (33). Down, Same as (Up) for normal fibroblast signature. (**B**) Same as in (**A**) by using specific signatures from each CAF-S1 cluster (see **Data S2**). GSEA analysis shows that clusters 0 (ecm-myCAF), 3 (TGFβ-myCAF) and 4 (wound-myCAF) are significantly associated with non-responders (Up), while clusters 1 (detox-iCAF), 2(IL-iCAF) and 5 (IFNγ-iCAF) are not (Down). (**C**) Expression assessed by the average z-score of each CAF-S1 cluster signature in responders and non-responders melanoma patients. (**D, E**) Same as in (**C**) using normal fibroblast signature and cytolytic index. (**F**) Responders and non-responders stratified in low- and high-CAF-S1 cluster expression (based on the third quartile of CAF cluster z-score). (**G, H**) Same as in (**F**) using normal fibroblast signature and cytolytic index. (**I**) Same as in (**A**) testing PPFE samples isolated before anti-PD-1 treatment from a cohort of 79 NSCLC patients (N = 48 non-responders and N = 22 responders) (**Table S2, cohort 4**). (**J**) Same as in (**B**) analyzing NSCLC cohort of patients.

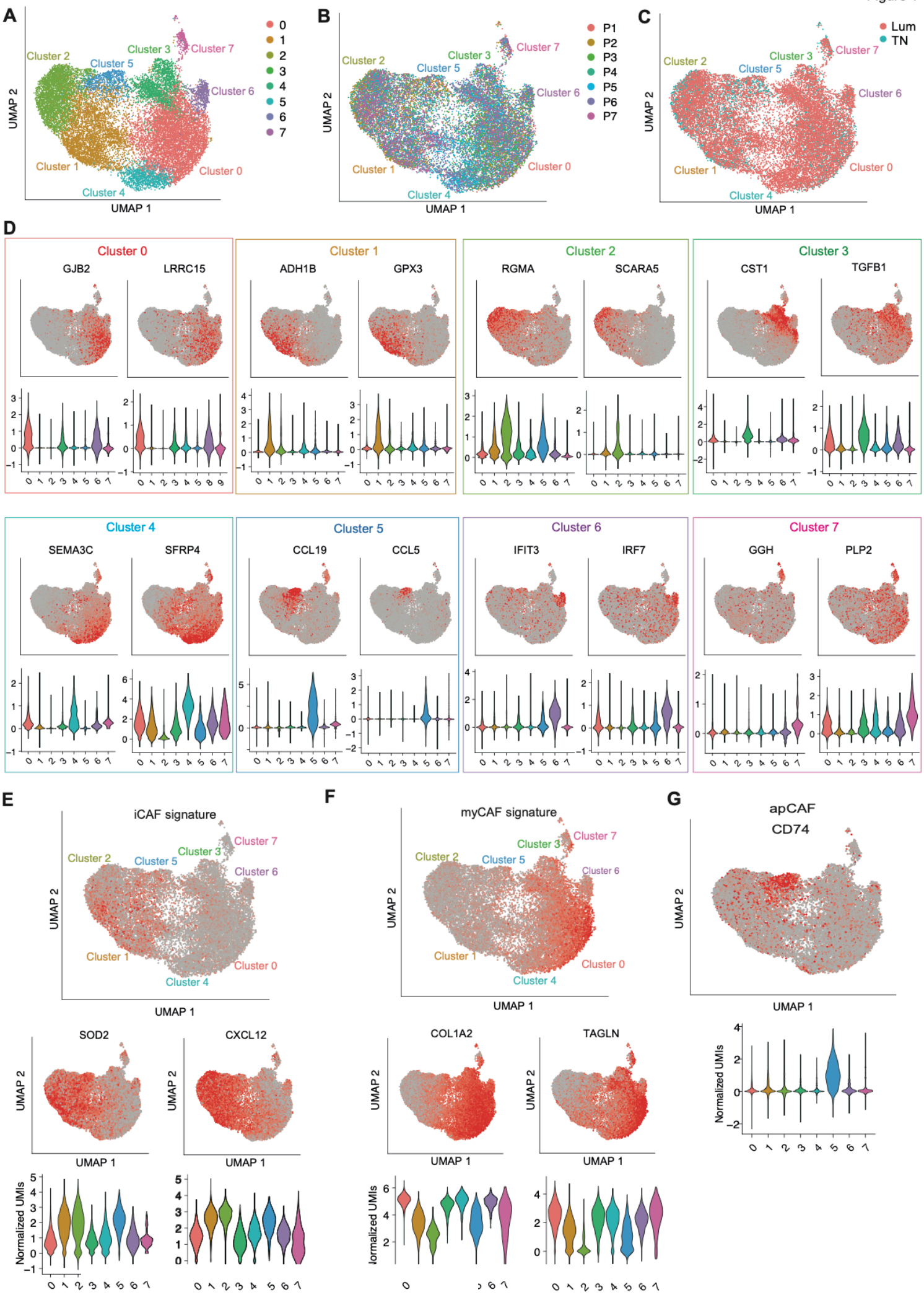
A
B
C
D
E
F
G
UMAP 1
UMAP 2
Cluster 0
Cluster 1
Cluster 2
Cluster 3
Cluster 4
Cluster 5
Cluster 6
Cluster 7
P1
P2
P3
P4
P5
P6
P7
Lum
TN
GJB2
LRRC15
ADH1B
GPX3
RGMA
SCARA5
CST1
TGFB1
SEMA3C
SFRP4
CCL19
CCL5
IFIT3
IRF7
GGH
PLP2
iCAF signature
myCAF signature
apCAF
CD74
SOD2
CXCL12
COL1A2
TAGLN
Normalized UMIs

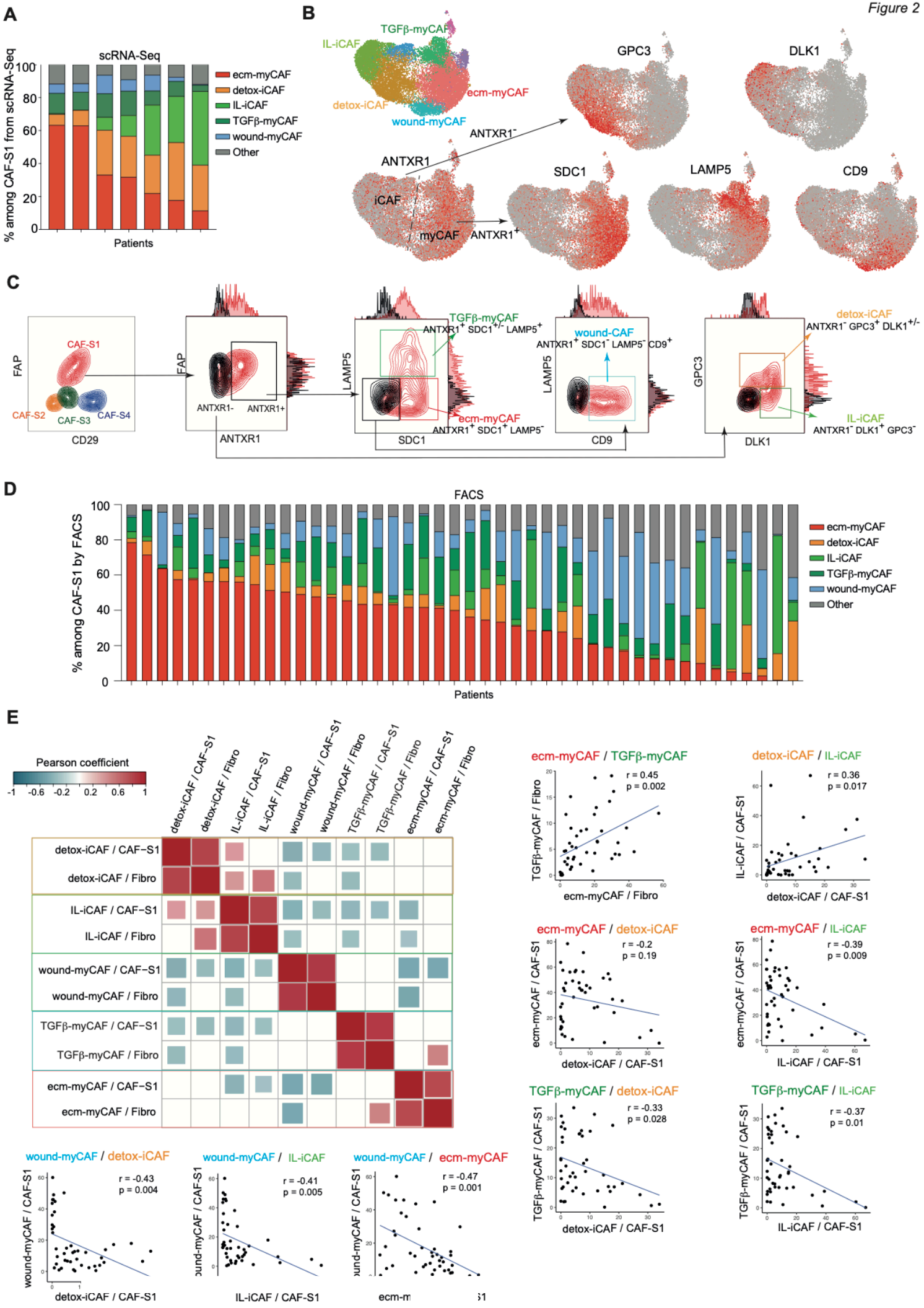
A
scRNA-Seq
% among CAF-S1 from scRNA-Seq
Patients
ecm-myCAF
detox-iCAF
IL-iCAF
TGFβ-myCAF
wound-myCAF
Other
B
TGFβ-myCAF
IL-iCAF
detox-iCAF
ecm-myCAF
wound-myCAF
ANTXR1⁻
ANTXR1
iCAF
myCAF
ANTXR1⁺
GPC3
DLK1
SDC1
LAMP5
CD9
C
FAP
CAF-S1
CAF-S2
CAF-S3
CAF-S4
CD29
ANTXR1-
ANTXR1+
ANTXR1
LAMP5
SDC1
TGFβ-myCAF
ANTXR1⁺ SDC1⁺/⁻ LAMP5⁺
ecm-myCAF
ANTXR1⁺ SDC1⁺ LAMP5⁻
wound-CAF
ANTXR1⁺ SDC1⁻ LAMP5⁻ CD9⁺
CD9
GPC3
DLK1
detox-iCAF
ANTXR1⁻ GPC3⁺ DLK1⁺/⁻
IL-iCAF
ANTXR1⁻ DLK1⁺ GPC3⁻
D
FACS
% among CAF-S1 by FACS
Patients
ecm-myCAF
detox-iCAF
IL-iCAF
TGFβ-myCAF
wound-myCAF
Other
E
Pearson coefficient
-1 -0.6 -0.2 0.2 0.6 1
detox-iCAF / CAF−S1
detox-iCAF / Fibro
IL-iCAF / CAF−S1
IL-iCAF / Fibro
wound-myCAF / CAF−S1
wound-myCAF / Fibro
TGFβ-myCAF / CAF−S1
TGFβ-myCAF / Fibro
ecm-myCAF / CAF−S1
ecm-myCAF / Fibro
ecm-myCAF / TGFβ-myCAF
r = 0.45
p = 0.002
TGFβ-myCAF / Fibro
ecm-myCAF / Fibro
detox-iCAF / IL-iCAF
r = 0.36
p = 0.017
IL-iCAF / CAF-S1
detox-iCAF / CAF-S1
ecm-myCAF / detox-iCAF
r = -0.2
p = 0.19
ecm-myCAF / CAF-S1
detox-iCAF / CAF-S1
ecm-myCAF / IL-iCAF
r = -0.39
p = 0.009
ecm-myCAF / CAF-S1
IL-iCAF / CAF-S1
TGFβ-myCAF / detox-iCAF
r = -0.33
p = 0.028
TGFβ-myCAF / CAF-S1
detox-iCAF / CAF-S1
TGFβ-myCAF / IL-iCAF
r = -0.37
p = 0.01
TGFβ-myCAF / CAF-S1
IL-iCAF / CAF-S1
wound-myCAF / detox-iCAF
r = -0.43
p = 0.004
wound-myCAF / CAF-S1
detox-iCAF / CAF-S1
wound-myCAF / IL-iCAF
r = -0.41
p = 0.005
IL-iCAF / CAF-S1
wound-myCAF / ecm-myCAF
r = -0.47
p = 0.001
ecm-myCAF / CAF-S1

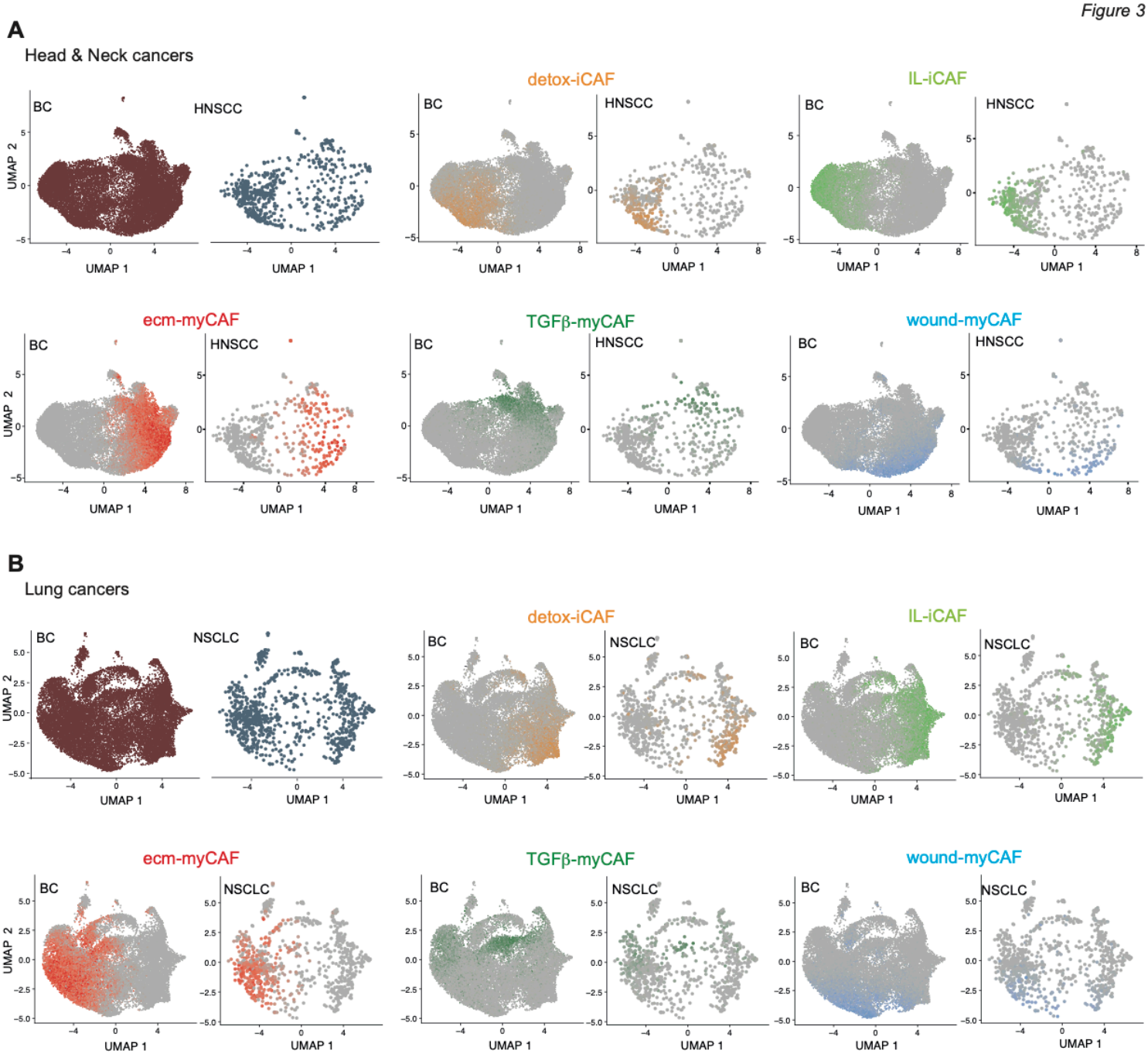
A
Head & Neck cancers
BC
HNSCC
detox-iCAF
IL-iCAF
ecm-myCAF
TGFβ-myCAF
wound-myCAF
UMAP 1
UMAP 2
B
Lung cancers
NSCLC

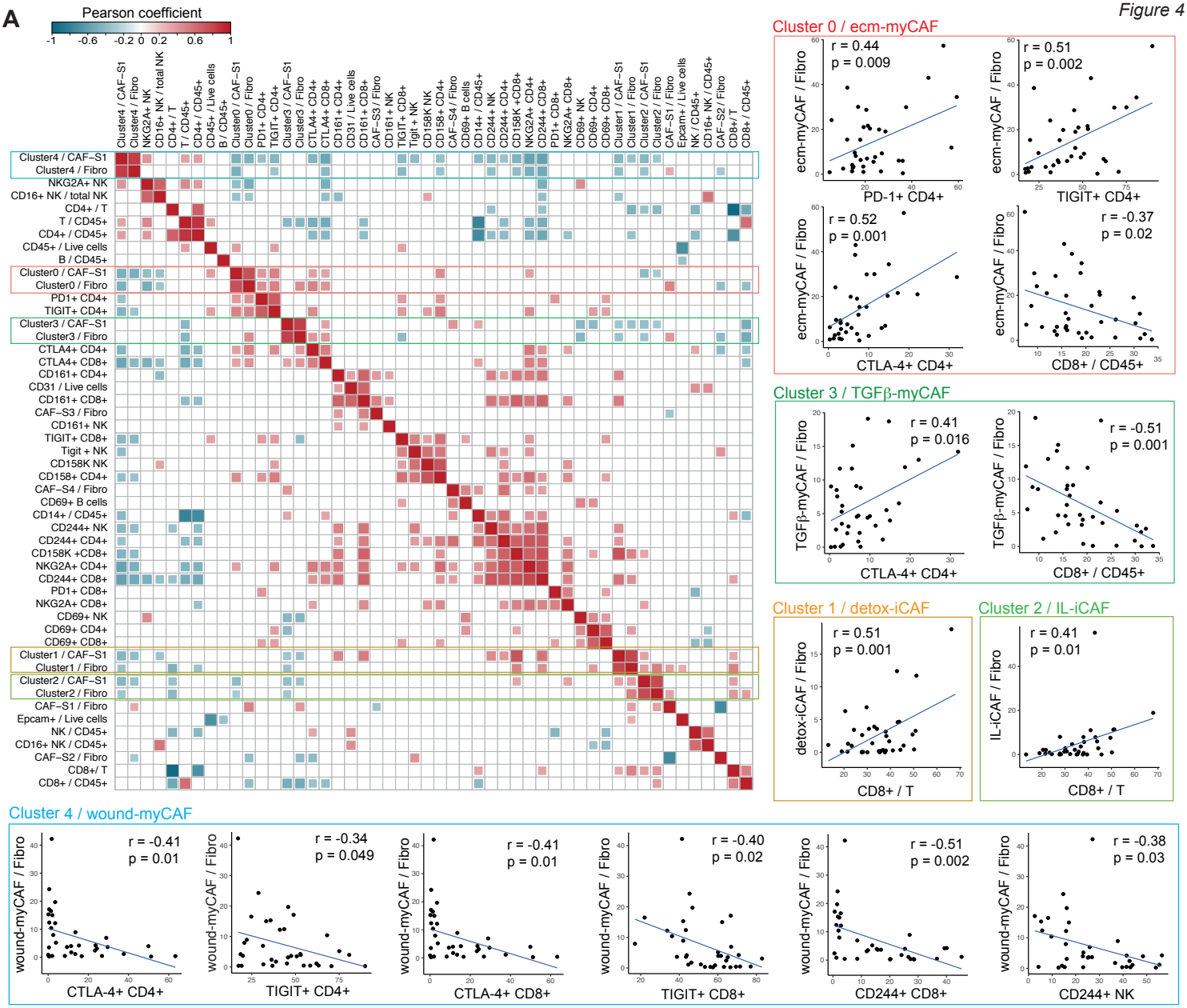

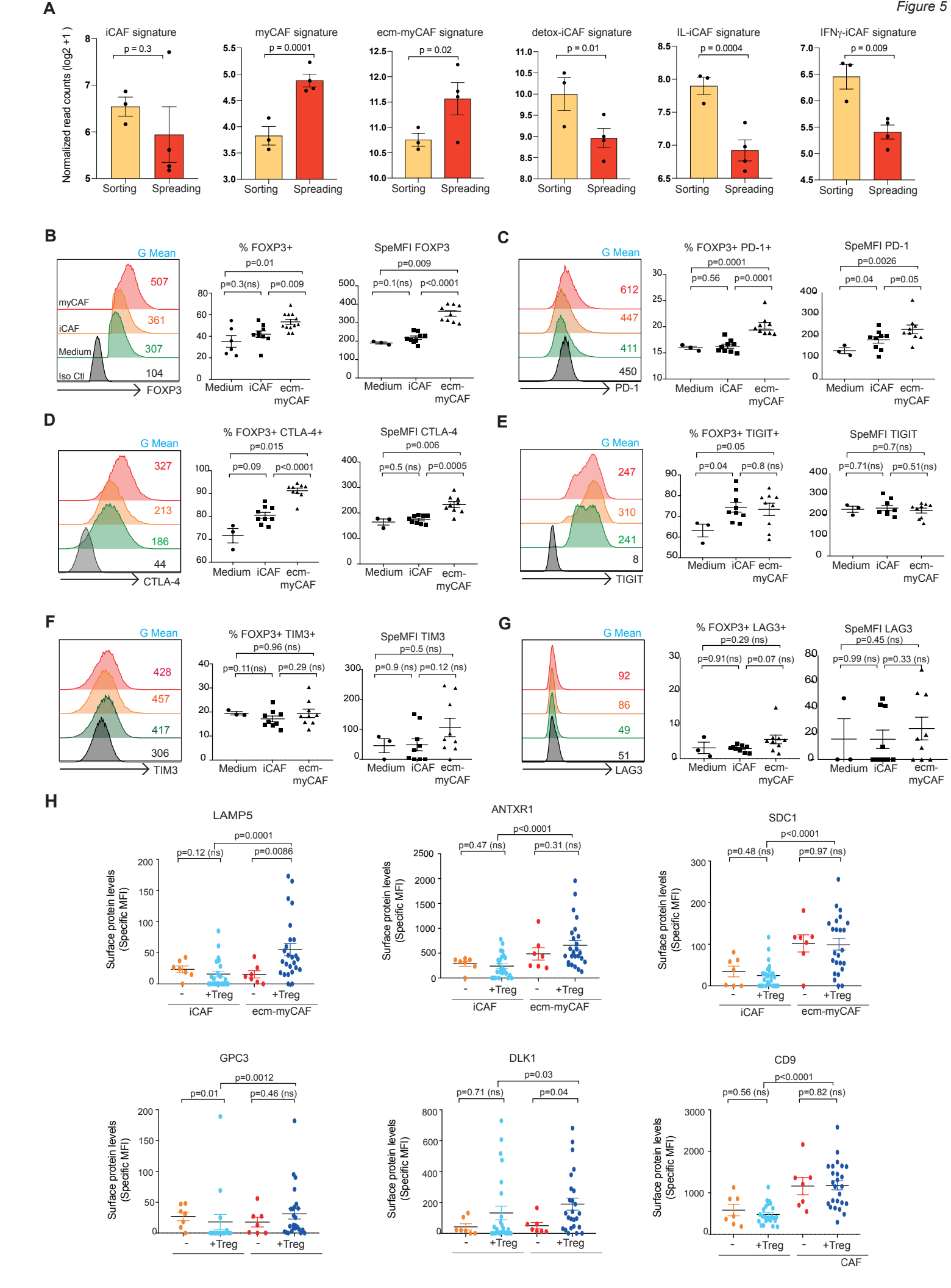
A
iCAF signature
myCAF signature
ecm-myCAF signature
detox-iCAF signature
IL-iCAF signature
IFNγ-iCAF signature
Normalized read counts (log2 +1)
p = 0.3
p = 0.0001
p = 0.02
p = 0.01
p = 0.0004
p = 0.009
Sorting
Spreading
B
G Mean
% FOXP3+
SpeMFI FOXP3
myCAF
iCAF
Medium
Iso Ctl
507
361
307
104
FOXP3
p=0.01
p=0.3(ns)
p=0.009
p=0.1(ns)
p<0.0001
Medium
iCAF
ecm-myCAF
C
G Mean
% FOXP3+ PD-1+
SpeMFI PD-1
612
447
411
450
PD-1
p=0.0001
p=0.56
p=0.0001
p=0.0026
p=0.04
p=0.05
D
G Mean
% FOXP3+ CTLA-4+
SpeMFI CTLA-4
327
213
186
44
CTLA-4
p=0.015
p=0.09
p<0.0001
p=0.006
p=0.5 (ns)
p=0.0005
E
G Mean
% FOXP3+ TIGIT+
SpeMFI TIGIT
247
310
241
8
TIGIT
p=0.05
p=0.04
p=0.8 (ns)
p=0.7(ns)
p=0.71(ns)
p=0.51(ns)
F
G Mean
% FOXP3+ TIM3+
SpeMFI TIM3
428
457
417
306
TIM3
p=0.96 (ns)
p=0.11(ns)
p=0.29 (ns)
p=0.5 (ns)
p=0.9 (ns)
p=0.12 (ns)
G
G Mean
% FOXP3+ LAG3+
SpeMFI LAG3
92
86
49
51
LAG3
p=0.29 (ns)
p=0.91(ns)
p=0.07 (ns)
p=0.45 (ns)
p=0.99 (ns)
p=0.33 (ns)
H
LAMP5
ANTXR1
SDC1
GPC3
DLK1
CD9
Surface protein levels (Specific MFI)
p=0.0001
p=0.12 (ns)
p=0.0086
p<0.0001
p=0.47 (ns)
p=0.31 (ns)
p<0.0001
p=0.48 (ns)
p=0.97 (ns)
p=0.0012
p=0.01
p=0.46 (ns)
p=0.03
p=0.71 (ns)
p=0.04
p<0.0001
p=0.56 (ns)
p=0.82 (ns)
-
+Treg
iCAF
ecm-myCAF
CAF

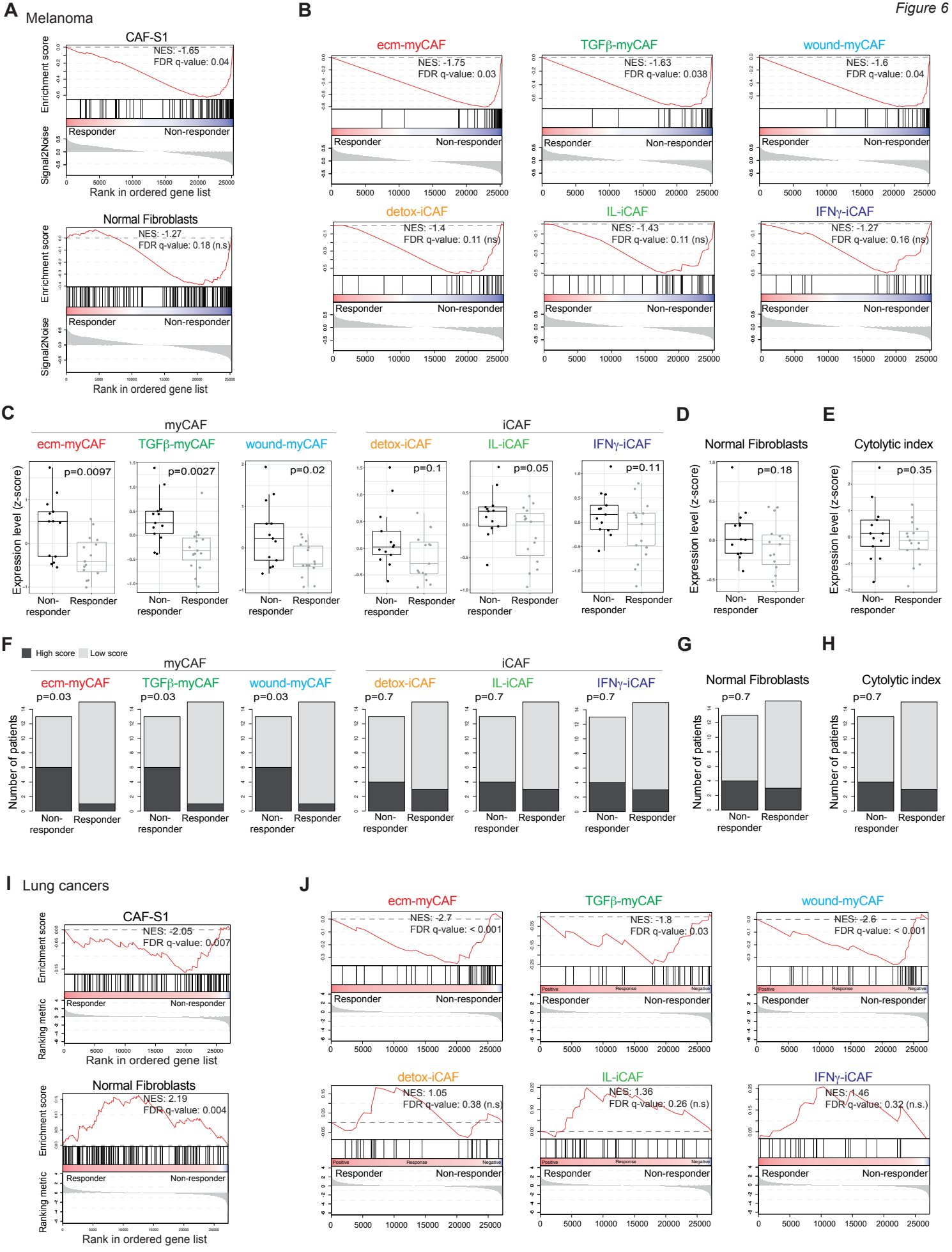
A
Melanoma
CAF-S1
NES: -1.65
FDR q-value: 0.04
Enrichment score
Responder
Non-responder
Signal2Noise
Rank in ordered gene list
Normal Fibroblasts
NES: -1.27
FDR q-value: 0.18 (n.s)
B
ecm-myCAF
NES: -1.75
FDR q-value: 0.03
TGFβ-myCAF
NES: -1.63
FDR q-value: 0.038
wound-myCAF
NES: -1.6
FDR q-value: 0.04
detox-iCAF
NES: -1.4
FDR q-value: 0.11 (ns)
IL-iCAF
NES: -1.43
FDR q-value: 0.11 (ns)
IFNγ-iCAF
NES: -1.27
FDR q-value: 0.16 (ns)
C
myCAF
iCAF
ecm-myCAF
TGFβ-myCAF
wound-myCAF
detox-iCAF
IL-iCAF
IFNγ-iCAF
p=0.0097
p=0.0027
p=0.02
p=0.1
p=0.05
p=0.11
Expression level (z-score)
Non-responder
Responder
D
Normal Fibroblasts
p=0.18
E
Cytolytic index
p=0.35
F
High score
Low score
p=0.03
p=0.7
Number of patients
G
H
I
Lung cancers
CAF-S1
NES: -2.05
FDR q-value: 0.007
Ranking metric
Normal Fibroblasts
NES: 2.19
FDR q-value: 0.004
J
ecm-myCAF
NES: -2.7
FDR q-value: < 0.001
TGFβ-myCAF
NES: -1.8
FDR q-value: 0.03
wound-myCAF
NES: -2.6
FDR q-value: < 0.001
detox-iCAF
NES: 1.05
FDR q-value: 0.38 (n.s)
IL-iCAF
NES: 1.36
FDR q-value: 0.26 (n.s)
IFNγ-iCAF
NES: 1.46
FDR q-value: 0.32 (n.s.)

AACR American Association for Cancer Research

CANCER DISCOVERY

Single-cell analysis reveals fibroblast clusters linked to immunotherapy resistance in cancer

Yann Kieffer, Hocine R Hocine, Geraldine Gentric, et al.

Cancer Discov Published OnlineFirst May 20, 2020.